04/07/2020

submitted

Phase separation of proSAAS into spheres results in core sequestration of TDP-43$^{216-414}$ aggregates

Juan R. Peinado[1,2], Kriti Chaplot[2], Timothy S. Jarvela[2],

Edward Barbieri[3], James Shorter[3] and Iris Lindberg[2]

[1:] Current address: Department of Medical Sciences, Ciudad Real Medical School, Oxidative Stress and Neurodegeneration Group, Regional Center for Biomedical Research, University of Castilla-La Mancha (UCLM), Ciudad Real, Spain

[2:] Department of Anatomy and Neurobiology, University of Maryland School of Medicine, University of Maryland, Baltimore, MD 21201 USA

[3.] Department of Biochemistry and Biophysics, Perelman School of Medicine, University of Pennsylvania, Philadelphia, PA 19104, USA

To whom correspondence should be addressed:

Iris Lindberg, Ph.D.

Department of Anatomy and Neurobiology

University of Maryland School of Medicine

20 Penn St, HSF2, S267

Baltimore, MD 21201

Phone 410 706 4778

Email: ilindberg@som.umaryland.edu

SUMMARY

Chaperone proteins perform vital functions in the maintenance of cellular proteostasis and play important roles during the development of neurodegenerative diseases involving protein aggregation. We have previously reported that a secreted neuronal chaperone known as proSAAS exhibits potent chaperone activity *in vitro* against protein aggregation and blocks the cytotoxic effects of amyloid and α-synuclein oligomers. Here we report that overexpression of proSAAS generates dense, membraneless 2 μm spheres which can increase by fusion up to 4 μM during expression within the cytoplasm. The presence of dense proSAAS spheres was confirmed using electron microscopy. ProSAAS spheres selectively sequestered GFP-TDP-43$^{216-414}$ within their cores, resulting in cellular redistribution and retardation of degradation. ProSAAS expression was protective against TDP-43 cytotoxicity in a yeast model system. Aggregate sequestration via proSAAS encapsulation may provide protection from cell-to-cell transmission of aggregates and explain the as-yet unclear mechanism underlying the cytoprotective chaperone action of proSAAS.

Keywords: ***proSAAS, PCSK1N, neurodegeneration, chaperone, TDP-43, neurodegeneration, proteostasis, liquid-liquid phase separation, ALS, FTD***

INTRODUCTION

In recent years it has become increasingly apparent that aggregation of key proteins triggers or enhances the progression of neurodegenerative diseases, including Alzheimer's, Parkinson's, Huntington's diseases as well as amyotrophic lateral sclerosis (ALS). During disease progression, misfolded proteins, many containing intrinsically disordered domains, initiate a proteostatic cascade in which proteins are destabilized and precipitate, generating neurotoxic events that culminate in neuronal death (Klaips et al., 2018; Valastyan and Lindquist, 2014). Clear examples of proteins involved in neurotoxic protein aggregation are tau and beta amyloid, proteins which represent the major components of the two pathological aggregates in Alzheimer's disease. Similarly, aggregated alpha-synuclein (α-Syn) is the major component of the cellular hallmark of Parkinson's disease, Lewy bodies. In ALS and frontotemporal dementia (FTD) the RNA-binding protein TDP-43, which normally shuttles between the cytoplasm and nucleus, is mislocalized to cytoplasmic aggregates (Ayala et al., 2008). In more than 90% of patients with ALS, and in 45% of those with FTD, the aggregation-prone carboxy-terminal domain of TDP-43, TDP-43$^{216-414}$ is cleaved off and forms abnormal cytoplasmic aggregates in both neurons and glia (Neumann et al., 2006). Lastly, in Huntington's disease a mutation in the HTT gene (also known as IT15) results in an abnormal increase in the number of internal CAG nucleotide repeats. As a result, the translated huntingtin protein contains disease-causing glutamine expansions (polyQ) that render it prone to misfolding and aggregation (reviewed in (Arrasate and Finkbeiner, 2012)). Many of these disease-linked proteins undergo liquid-liquid phase separation (LLPS) en route to formation of solid phase aggregates (eg (Gasset-Rosa et al., 2019)). LLPS is thought to be important to proteostatic control during cellular stress (Gomes and Shorter, 2019).

Increasing evidence also points to important roles for cellular and secreted chaperones in the formation and deposition of abnormal protein aggregates in neurodegenerative disease [reviewed in (Bobori et al., 2017; Chiti and Dobson, 2017; Hartl, 2017; Klaips et al., 2018)]. Chaperone proteins may act to sequester misfolded proteins; refold unfolded proteins; and cooperate with degradative machinery, either directly or indirectly, to facilitate the degradation of misfolded species and/or enhance disaggregation (see above reviews). Overexpression of cytoplasmic chaperones has been shown to mitigate aggregate toxicity (Balchin et al., 2016; Klaips et al., 2018; Webster et al., 2019), while overexpression of the constitutively-secreted secretory chaperones clusterin and α2-macroglobulin is neuroprotective in Neuro2A cells ((Whiten et al., 2018); reviewed in (Foster et al., 2019)).

Despite the enhanced susceptibility of neurons to proteostatic disease, few neural-specific chaperones have been identified in brain tissue. We have previously reported that a neuronal secretory chaperone, proSAAS, potently blocks the aggregation of neurodegenerative disease-related proteins. Using *in vitro* assays, we showed that recombinant proSAAS blocks the assembly of both β-amyloid and α-Syn aggregation into fibrils, and is cytoprotective against oligomers of these two proteins (Hoshino et al., 2014; Jarvela et al., 2016). The likelihood of an important role for proSAAS in processes related to neurodegenerative disease is supported by the observation that proSAAS immunoreactivity colocalizes with inclusion bodies in a variety of neurodegenerative diseases (Hoshino et al., 2014; Jarvela et al., 2016; Kikuchi et al., 2003; Wada et al., 2004). Lastly, thus far seven independent proteomics studies have identified proSAAS as a differentially expressed biomarker in cerebrospinal fluid obtained from Alzheimer's disease patients (Abdi et al., 2006; Choi et al., 2013; Finehout et al., 2007; Holtta et al., 2015; Jahn et al., 2011; Spellman et al., 2015; Wang et al., 2016), and transcriptomics studies of Alzheimer's brain

tissue show that proSAAS expression increases during disease progression (Mathys et al., 2019). These data have prompted us to investigate a potential role for the proSAAS chaperone in handling misfolded proteins involved in neurodegeneration-related aggregation in living cells. To that end we have here investigated the effect of proSAAS expression on specific protein variants of tau, α-Syn, TDP-43, and huntingtin, all of which are known to aggregate in neurons during neurodegenerative disease progression. Unexpectedly, we found that cytoplasmic expression of proSAAS results in the formation of unique spherical structures that appear to selectively recruit and sequester TDP-$43^{216-414}$ aggregates.

RESULTS

Development of cellular systems to study protein aggregation

To explore the activity of proSAAS as an anti-aggregant chaperone, we first characterized the expression patterns of proteins susceptible to aggregation in HEK and Neuro2A cells. Specifically, we tested various constructs expressing TDP-43, HTT, Tau, and α-Syn, all of which represent proteins prone to aggregation in neurodegenerative disease (see *Materials and Methods* for specific construct descriptions). **Figure 1A-C** depicts the aggregation of these proteins in cells of non-neuronal (HEK) and neuronal (Neuro2A) origin. GFP-tagged TDP-$43^{216-414}$ (**Figure 1A**) and HA-tagged HTT-Q74 (**Figure 1B**) formed aggregates when transfected into either cell line, similar to those previously reported in motor neuron-like NSC-34 cells (Yang et al., 2010) and PC12 cells (Furlong et al., 2000). In both HEK and Neuro2A cells, TDP-$43^{216-414}$ aggregates appeared as small intense puncta dispersed throughout the cytosol (**Figure 1A**). In contrast, HTT-Q74 was expressed as amorphous aggregates (**Figure 1B**). Interestingly, and contrary to results with HTT-Q74, GFP-HTT-Q74 formed large, highly intense aggregates in HEK cells (**Figure 1C, right top**), but exhibited dispersed fluorescence when expressed in Neuro2A (**Figure 1C, right bottom**). These differences in the expression pattern of aggregating proteins in these two cell lines prompted us to continue our study using both lines.

We assessed the percent of cells showing aggregates following 24 h of transfection of different constructs. TDP-$43^{216-414}$ aggregates were observed in approximately 10 $\pm$ 2% of transfected HEK cells and 2.0 $\pm$ 0.6% of transfected Neuro2A cells. HTT-Q74 aggregates were found in 19 $\pm$ 3% of HEK cells and 11 $\pm$ 3% of Neuro2A cells (mean $\pm$ SD, n=3 counts, 200 cells per construct). Wild-type Tau and human α-Syn and their modified constructs, which reportedly form aggregates (TauE14 and α-Syn A53T; (Furlong et al., 2000; Hoover et al., 2010)) were also tested, but did not form aggregates in either HEK or Neuro2A cells; instead, widespread cytosolic distribution was seen (data not shown). No combinations of TDP-$43^{216-414}$ or HTT-Q74 with Tau or α–Syn resulted in visible aggregates of these latter two proteins (results not shown). Thus, we focused our efforts on potential proSAAS chaperone interactions using TDP-$43^{216-414}$ and HTT-Q74 aggregates.

Expression of secretory proSAAS, but not clusterin, results in the formation of small spheres

At 24 h following transfection, expression of the secretory chaperone proSAAS in HEK and Neuro2A cells resulted in a punctate signal dispersed throughout the cell, possibly corresponding to the known targeting of this protein to secretory granules (Wardman and Fricker, 2014) (**Figure 1D**). In addition to this widespread signal, 24 h after transfection, approximately 1% of HEK cells displayed multiple proSAAS spheres immunoreactive with FLAG antiserum (arrow**; Figure 1D**). Forty-eight h after transfection, these spheres, which occasionally

grew up to 2 μm in diameter, were found in 25% of transfected HEK cells **(Figure S1A, upper row**). In contrast, at 48 h after transfection, Neuro2A cells contained small proSAAS-immunoreactive puncta rather than spheres (**Figure S1A, lower row**); proSAAS was also detected in cell culture media, suggesting efficient secretion (data not shown; see also (Hoshino et al., 2014)). Co-transfection of proSAAS with cDNA encoding Cherry-CART, a secretory granule marker (Blanco et al., 2015) revealed no colocalization with proSAAS-immunoreactivity in either HEK (**Figure S1B, upper row**) or Neuro2A cells (**Figure S1B, lower row**), and the diameters of proSAAS-immunoreactive granules were markedly larger than those of Cherry-CART in both cell lines (**Figure S1B**), implying segregation of the two secreted components. Segregation of the various portions of proSAAS within different secretory granules has been previously documented in AtT-20 cells (Wardman and Fricker, 2014).

We also characterized the expression pattern of the secretory chaperone clusterin, as it has been reported that upon ER stress this chaperone is retrotranslocated from the ER/ Golgi to the cytoplasm (Nizard et al., 2007), where it binds TDP-43$^{216-414}$ (Gregory et al., 2017). In HEK cells, FLAG-tagged clusterin immunoreactivity was widely distributed (**Figure 1E, upper row**), while in Neuro2A cells, clusterin showed intense localization in a small area adjacent to the nucleus (**Figure 1E, lower row**), presumably corresponding to the Golgi region.

Treatment of cells with thapsigargin enhances clusterin's anti-aggregant effect

In order to evaluate the effect of proSAAS and clusterin on protein aggregation, we co-expressed cDNAs encoding these FLAG-tagged chaperones together with HTT-Q74 and TDP-43$^{216-414}$. In HEK cells, HTT-Q74 aggregates did not colocalize with either cotransfected proSAAS (**Figure S1C, upper row**) or with clusterin (**Figure S1C, lower row**)**;** similar results were also obtained following expression of a vector encoding GFP**-**HTT-Q74 in Neuro2A cells (data not shown)**.**

Co-expression of proSAAS did not alter the distribution or the intensity of TDP-43$^{216-414}$ aggregates in either HEK (**Figure S2A, upper row**) or Neuro2A cells (data not shown) and no colocalization of proSAAS with aggregates was observed. While clusterin expression did impact the distribution of TDP-43$^{216-414}$ aggregates, which became highly distributed through the cytosol in both cell lines (as shown in **Figure S2A; and Figure 2A, bottom row**), it did not reduce the cellular intensity of the fluorescence associated with the aggregates (**Figure S2C**). In both Neuro2A and HEK cells, clusterin immunoreactivity was located in the cell periphery in both HEK and Neuro2A cells, although its actual colocalization with TDP-43$^{216-414}$ was limited.

To evaluate potential effects on TDP-43$^{216-414}$ aggregate formation following cell stress, we tested both clusterin and proSAAS in cells treated with a low concentration (12.5 nM) of the ER stressor thapsigargin, a drug which depletes ER calcium. We found differential effects in HEK and Neuro2A cells. In thapsigargin-treated HEK cells, clusterin significantly ($p<0.05$) decreased the fluorescence associated with TDP-43$^{216-414}$ aggregates as compared to the TDP-43$^{216-414}$ signal observed in the absence of drug (**Figure S2B, bottom row; and Figure S2D**); and in treated Neuro2A cells, clusterin expression completely abolished the formation of TDP-43$^{216-414}$ aggregates (data not shown). Furthermore, in thapsigargin-treated HEK cells, clusterin exhibited increased co-localization with TDP-43$^{216-414}$ (**Figure S2B, lower panel**); this evidence of cytoplasmic retrotranslocation is in agreement with the results of others (Gregory et al., 2017).

In contrast, proSAAS co-expression in the presence of thapsigargin did not alter the distribution of TDP-43$^{216-414}$ aggregates in either HEK cells (**Figure S2B, middle panel**) or Neuro2A cells (not shown). However, a small number of differentiated cells, as judged by extensive

neurite formation, showed intense colocalization of proSAAS and TDP-43$^{216-414}$ within neurites (**Figure 2B, lower *vs* upper panels**), an effect confirmed in 3 independent experiments.

Cytosolic expression of proSAAS results in the formation of immunoreactive spherical structures both in cell lines and in primary neurons

To investigate the potential effect of proSAAS following direct contact with cytoplasmic protein aggregates, we expressed FLAG-tagged proSAAS lacking a signal peptide ("cyto-proSAAS") in Neuro2A and HEK cells. Surprisingly, in both cell lines, this resulted in the appearance of FLAG-tagged immunoreactive spherical structures dispersed throughout the cytosol which were similar to those found for secretory proSAAS, but larger; they were easily observable at 40x using phase-contrast microscopy (**Figure S3A**). Confocal microscopy using anti-FLAG staining confirmed the proSAAS origin of the spherical structures in both Neuro2A (**Figure 3A**) and HEK cells **(Figure S3B**). Western blotting of cyto-proSAAS-transfected HEK cells revealed the expected band of approximately 30 kDa, corresponding to full-length proSAAS (**Figure S3A**). Interestingly, 24 h after transfection of cyto-proSAAS cDNA, 90% of the Neuro2A cells exhibited cyto-proSAAS immunofluorescence, expressed mostly as one sphere per cell (**Figure 3A, left**). These spheres exhibited an average size of 2 ± 1 μm. Similar results were found for HEK cells at 24 h, though the size of the spheres was greater, with an average diameter of 4 ± 2 μm. This pattern of expression remained constant at 48 h in Neuro2A (**Figure 3A, right)**, and in HEK cells the size of the spheres increased at this timepoint (**Figure S3B, right).**

Lastly, we transfected primary hippocampal cells to determine whether sphere production was an artifact of tumor cell lines or could also be observed in primary cells. Although transfection efficiency was low, we were also able to observe the expression of cyto-proSAAS spheres in transfected hippocampal neurons (**Figure S3C**), again mostly showing only one sphere one cell.

To determine whether these spherical structures are unique to the proSAAS sequence or whether other secretory chaperones delivered to the cytoplasm would perform similarly, we tested 7B2, a similarly-sized but unrelated chaperone protein which exhibits potent anti-aggregant activity against the proPC2 convertase as well as other aggregating proteins (Helwig et al., 2013; Lee and Lindberg, 2008). However, expression of signal-less FLAG-tagged 7B2 never resulted in cytoplasmic sphere generation, and 7B2-FLAG immunoreactivity was found mostly in the periphery of the cytoplasm in both Neuro2A and HEK cells (**Figure S3D).**

Cytoplasmic proSAAS spheres incorporate TDP-43$^{216-414}$ aggregates within their cores upon direct contact

Co-expression of cytosolic proSAAS with TDP-43$^{216-414}$ profoundly altered the distribution of TDP-43$^{216-414}$ aggregates. Remarkably, rather than the usual dispersed distribution, TDP-43$^{216-414}$ aggregate fluorescence expressed in the presence of cytosolic proSAAS was located mostly within the cores of the proSAAS spheres. This occurred both in Neuro2A (**Figure 3B, upper row**) and HEK cells (**Figure S4A,B).** Recruitment of TDP-43$^{216-414}$ proteins into proSAAS spheres occurred exclusively with TDP-43$^{216-414}$ aggregates, as neither HA-tagged HTT-Q74 nor EGFP-HTT-Q74 (**Figure 3B, middle row and Figure S4, C-D**) aggregates were incorporated**.** Co-expression of cyto-proSAAS with the non-aggregating cytosolic protein mCherry, which was distributed homogenously in the cytosol of both Neuro2A and HEK cells, also did not result in mCherry incorporation into the spheres (**Figure 3B, lower row and Figure S4E)**. Given the functional and structural similarities of TDP-43 and FUS, both DNA/RNA binding proteins (Mackenzie et al.,

2010), we investigated the idea that FUS could also be recruited to cyto-proSAAS spheres; however, no GFP-tagged FUS was observed inside the spheres (data not shown).

To identify the specific region of TDP-43 responsible for the entry into cyto-proSAAS spheres, we overexpressed four additional constructs together with cyto-proSAAS, each consisting of different protein domains (see scheme in **Figure S5A**). Similarly to TDP-$43^{216-414}$, the C-terminal fragments, TDP-43^{86-414} (**Figure S5B**) and TDP-$43^{170-414}$ (**Figure S5C**) both formed cytosolic aggregates which were efficiently incorporated into proSAAS spheres. Interestingly, these are the only TDP-43 constructs which contain the prion-like domain (Cushman et al., 2010). In contrast, the N-terminal fragments, GFP-TDP-43^{1-193} and GFP-TDP-43^{1-274} immunofluorescence was concentrated in the nucleus and did not form aggregates; and no fluorescence from these constructs was observed inside cyto-proSAAS spheres (data not shown).

Analysis of the patterns of cyto-proSAAS/ TDP-$43^{216-414}$ expression in both cell lines revealed consistent displacement of the TDP-$43^{216-414}$ fluorescent signal from the cytosol to the spheres. A representative expression pattern for HEK cells is shown in **Figure 4A-D**. The dispersed cytosolic distribution of TDP-$43^{216-414}$ aggregates almost completely disappeared upon coexpression of cyto-proSAAS, and the most abundant pattern of distribution corresponded to that depicted in **Figure 4A** with the formation of one sphere/cell containing all cellular immunofluorescent TDP-$43^{216-414}$. Quantitative cell imaging demonstrated that 93% of HEK cells (**Figure 4A**) matched this pattern. The remaining 7% of cyto-proSAAS-expressing cells corresponded either to cells showing a portion of the TDP-$43^{216-414}$ signal inside the sphere and a portion outside, in an intense aggregate juxtaposed to the spheres **(Figure 4B,C**); or to cells exhibiting small spheres with the majority of the TDP-$43^{216-414}$ signal inside, but with the simultaneous presence of scattered cytosolic TDP-$43^{216-414}$ aggregates (**Figure 4D**). Similar results were found in Neuro2A cells (data not shown).

Figure 4E shows a higher magnification of a cell containing TDP-$43^{216-414}$ aggregates near and/or directly apposing cyto-proSAAS spheres. To permit quantitative and qualitative comparisons of the characteristics of TDP-$43^{216-414}$ aggregates in the core *vs* the exterior of the proSAAS spheres, we obtained Z-stacks of these cells (**Figure S5, D-F**). We observed that the surface area to volume ratio of TDP-43^{216-}414 aggregates found inside the spheres was significantly larger (i.e. more loosely packed/dispersed) than the aggregates outside the spheres (**Figure S5,D**). We also noted that the internal TDP-$43^{216-414}$ fluorescence, both mean pixel intensity (**Figure S5, E**) and total signal intensity (**Figure S5, F**), was significantly lower than that found in aggregates surrounding the spheres, indicating that possible disaggregation or controlled entry of the TDP-$43^{216-414}$ aggregates may take place within the sphere. Our finding that cyto-proSAAS was able to sequester aggregating proteins into spheres, even when these spheres are formed well after TDP-$43^{216-414}$ aggregate generation, supports the high affinity of TDP-$43^{216-414}$ aggregates for proSAAS spheres (**Figure S5G).**

ProSAAS spheres are very dense and exclude antibodies

We used transmission electron microscopy to gain a better structural understanding of proSAAS-TDP-$43^{216-414}$ spheres (**Figure 4 F,G**). When transfected alone, TDP-$43^{216-414}$ accumulated in small amorphous structures of 100 to 500 nm (**Figure 4F).** Cells transfected with both cyto-proSAAS and TDP-$43^{216-414}$ cDNA showed electron-dense spheres of the expected size, in agreement with immunofluorescence experiments (**Figure 4G).** The density of these spheres

did not permit visualization of the internal TDP-43$^{216-414}$ aggregates. Untransfected cells contained neither the small amorphous structures nor the spheres (data not shown).

The observation of highly dense spheres of cyto-proSAAS prompted us to investigate whether the proSAAS protein forms an impermeant shell which excludes entry of antibodies, thus resulting in the characteristic ring-like signal seen in **Figures 3 and 4** using anti-FLAG staining. To determine whether proSAAS spheres are impermeant to antibodies, we carried out immunohistochemistry against the TDP-43$^{216-414}$ protein rather than imaging this protein with its GFP tag. **Figure S6A** shows the total lack of TDP-43$^{216-414}$ staining using TDP-43 immunohistochemistry in proSAAS spheres (arrowheads) that clearly contain TDP-43$^{216-414}$ fluorescent protein. Anti-GFP staining gave similar results (data not shown). Thus, our lack of ability to detect HTT aggregates within proSAAS spheres using the anti-HA antibody does not provide definitive evidence that HTT is not encapsulated. However, when the same HTT construct was GFP-tagged, it was also not found within the proSAAS sphere core, as shown in **Figure S4, panel D**.

ProSAAS co-expression slows the kinetics of TDP-43$^{216-414}$ degradation

In order to examine the effect of proSAAS on the kinetics of TDP-43 degradation, cycloheximide was used to terminate protein synthesis during a 6h period following co-transfection of TDP-43$^{216-414}$ with cyto-proSAAS; Western blotting was employed to examine cellular TDP-43$^{216-414}$ forms over time. Interestingly, the half-life of intact TDP-43$^{216-414}$ was significantly increased upon co-expression of cyto-proSAAS (**Figure 5A**). More than 80% of the TDP-43$^{216-414}$ protein was degraded after 6 h, while 43% of this protein was still present at this time point following co-expression with cyto-proSAAS (**Figure 5A**). Cells untreated with cycloheximide showed similar levels of TDP-43$^{216-414}$ across the incubation time frame (data not shown). **Figure 5B** shows representative confocal images of HEK cells before (0 h) and after (6 h) cycloheximide treatment; these images support the increased persistence of TDP-43$^{216-414}$ fluorescence inside the proSAAS spheres.

To determine whether proSAAS-associated TDP43$^{216-414}$ aggregates are targeted for proteasomal degradation, we expressed an HA-tagged ubiquitin vector (UbK48-HA*;* (Lim et al., 2005) together with TDP43$^{216-414}$ and cyto-proSAAS vectors in HEK cells (**Figure 6A**). Using HA-directed antiserum, we found that cyto-proSAAS was not ubiquitinated, either when co-expressed with UBK48-HA alone (**Figure 6A, top row**) or in the added presence of TDP43$^{216-414}$ (**Figure 6A, bottom row**). However, TDP43$^{216-414}$ aggregates were ubiquitinated (*notched arrowheads,* **Figure 6A, middle row**), a previously reported feature of aggregated TDP43 (reviewed in (Dong and Chen, 2018)). Interestingly, when co-expressed with cyto-proSAAS in HEK cells, TDP43$^{216-414}$ aggregates apposing the spheres were highly ubiquitinated (*notched arrowheads*, **Figure 6A, bottom row**)**,** suggesting that ubiquitinated TDP43 might potentially be favored for entry into cyto-proSAAS spheres. However, likely owing to impermeability issues (see above), we could not detect any ubiquitin-HA signal from within the sphere core; thus this idea cannot be definitively confirmed.

Cytosolic proSAAS spheres do not correspond to known organelles

Using HEK cells, we attempted to determine whether cyto-proSAAS spheres correspond to a known organelle, or fuse with known organelles, by staining their surfaces with antisera directed against various cellular markers characteristic of different organelles. The absence of mCherry fluorescence inside the cyto-proSAAS spheres following co-expression of Cherry-LC3 precluded the idea that proSAAS spheres could have an autophagosomal origin or destination

(**Figure S6, B**). Antisera to the stress granule markers TIA1R and G3BP1 were similarly negative (data not shown). Markers of lysosomes (Lamp-1) or Golgi (giantin); (**Figure S6, C-D**) also failed to stain proSAAS spheres. While antisera against HSP70 gave slight positive immunostaining when compared to cells transfected with empty vector (**Figure S6, E**), this fluorescence was cytosolic rather attached to the spheres. Lysotracker staining also failed to label the structure (data not shown). In addition, the lipid stain Bodipy, and antisera to the membrane marker caveolin both failed to co-localize with these structures, indicating that they are not lipid-rich (data not shown).

To further understand the physiological relevance of the interaction between TDP43$^{216-414}$ and cyto-proSAAS, we explored the role of stress granules by transfecting cDNA encoding a known stress granule marker, PABPC4, in HEK cells. We observed diffuse staining against the HA tag in the absence of stressors (**Figure 6B, top row**). When the fluorescent TDP43$^{216-414}$ construct was co-expressed, PABPC4-positive stress granules formed in all GFP-positive cells. TDP43$^{216-414}$ aggregates were also positive for PABPC4 staining (*filled arrowheads*, **Figure 6B, middle row**). Cells expressing PABPC4 and treated with sodium arsenite (0.5 μM) for 30 min prior to fixing exhibited similar PABPC4 -positive stress granules (data not shown). Interestingly, when we co-expressed PABPC4 with cyto-proSAAS in the absence of TDP43$^{216-414}$, we again observed stress granule formation (**Figure 6B, bottom row**). PABPC4-marked stress granules appeared to be juxtaposed against the cyto-proSAAS spheres, without internal staining (possibly due to lack of antibody penetration into the spheres) (*empty arrowhead*, **Figure 6B, bottom row**). When PABPC4 was expressed together with secretory proSAAS or cyto-7B2, no such punctae were observed (data not shown). Triple expression of PABPC4, cyto-proSAAS and TDP43$^{216-414}$ consistently resulted in the presence of stress granules adjacent to TDP43$^{216-414}$-containing cyto-proSAAS spheres (data not shown). We conclude that cyto-proSAAS spheres can interact with stress granule proteins.

Cherry-cyto-proSAAS forms spheres only in the presence of excess cyto-proSAAS

We designed a construct of signal-less proSAAS containing an amino-terminal mCherry tag (Cherry-cyto-proSAAS) in order to obtain dynamic information regarding the interaction of TDP-43$^{216-414}$ aggregates with the cyto-proSAAS spheres as well as to investigate the dynamics of sphere formation. Surprisingly, rather than forming spheres, Cherry-cyto-proSAAS formed aggregates dispersed throughout the cytosol, indicating likely misfolding (**Figure 7A, top row**). Reducing the concentration of Cherry-cyto-proSAAS to one-sixth by dilution of cDNA with non-Cherry-containing cyto-proSAAS cDNA resulted in the capture of all of the dispersed mCherry signal within cyto-proSAAS spheres, in both Neuro2A and HEK cells, suggesting rescue of aggregate formation by non-tagged cyto-proSAAS. **Figure 7A, bottom row** depicts a representative Neuro2A cell. The fact that expression of excess cyto-proSAAS can efficiently block the cytosolic aggregation of Cherry-cyto-proSAAS supports the general anti-aggregant functions of proSAAS previously documented for Abeta 1-42, α-synuclein, and islet amyloid polypeptide (Hoshino et al., 2014; Jarvela et al., 2016; Peinado et al., 2013).

In vivo tracking of TDP-43$^{216-414}$ reveals dynamic interaction of aggregates with proSAAS spheres

To view the dynamics of cyto-proSAAS spheres, we performed widefield microscopy beginning 18 h after triple transfection with cDNAs encoding cyto-proSAAS, TDP-43$^{216-414}$, and mCherry-cyto-proSAAS (in the weight ratio 1:1: 0.2; see *Materials and Methods*) in HEK cells. The cyto-proSAAS spheres first formed as several smaller spheres before fusing into only a few large spheres per cell (**Figure S7A; Supplemental Movie**). Occasionally, but only rarely, we

observed full extrusion of TDP-43$^{216-414}$ aggregates from the center of cyto-proSAAS spheres (**Figure S7B**). When this occurred, the entirety of the TDP-43$^{216-414}$ content was removed over the course of 40 seconds, and then remained outside the cyto-proSAAS sphere.

Cyto-proSAAS expression is cytoprotective against TDP-43 in yeast cells

To assess the cytoprotective effects of proSAAS and 7B2 we tested these genes in a yeast model of TDP-43 toxicity **(Figure 7B, left side).** In this model, expression of the full-length TDP-43 and proSAAS transgenes are tightly controlled by a galactose-inducible promoter (pGAL1). The empty vector control showed strong TDP-43-mediated growth impairment on galactose agar after 48 h, whereas this toxicity was partially rescued by expression of proSAAS, cyto-proSAAS, and 7B2. We were unable to detect expression of cyto-7B2 via Western blotting (**Figure 7B, right side)** and correspondingly this construct did not rescue the TDP-43 toxicity. These data provide functional evidence for cytoprotection against full-length TDP-43 toxicity by proSAAS.

DISCUSSION

Prior work has shown that proSAAS, a small unglycosylated protein chaperone which contains no α-crystallin domain, is able to block and/or prevent the aggregation of proteins directly involved in neurodegenerative disorders, including Abeta and α-Syn (Hoshino et al., 2014; Jarvela et al., 2016). ProSAAS, found specifically in tissues such as neurons and endocrine cells which contain a regulated secretory pathway, has been found to be associated with plaques, Lewy bodies, and other brain aggregates in AD, PD and FTLD (Jarvela et al., 2016; Kikuchi et al., 2003). However, whether proSAAS directly affects the formation of intracellular aggregates has not been examined in living cells. In this study we have attempted to gain cellular, structural and functional information for proSAAS action in Neuro2A and HEK cells, and in primary neurons.

Two major findings were made in this study. The first is the discovery that delivery of proSAAS to the cytosol by expression of signal-less proSAAS (cyto-proSAAS) results in the ultimate formation of one unique symmetric sphere in the cytosol, formed by fusion of smaller spheres, and reminiscent of the smaller spheres formed in the secretory pathway. The second major finding is that these cyto-proSAAS spheres specifically interact with TDP-43$^{216-414}$ aggregates and efficiently sequester these aggregates from the cytosol within their cores.

Several attempts were made to gain information as to the composition of cyto-proSAAS spheres but failed due to the inability of antibodies to access the highly dense sphere interiors. The observation that the cyto-proSAAS sphere is a membrane-less structure able to efficiently fuse suggests that it arises during a condensation process in which the proSAAS protein spontaneously assembles into a spherical structure. While we confirmed the likely presence of proSAAS within the sphere core using a fluorescent form of this protein, reporters for traditional stress granule RNA components (such as G3BP1and TIA1R antisera) were negative with respect to the sphere shell. However, we cannot at present rule out the possibility that proSAAS spheres may contain these as well as other proteins and/or RNA. Our overexpression experiments using the stress granule marker PABP in the presence of cyto-proSAAS and TDP-43 support the idea of a close, but non-overlapping, physical relationship between stress granules and cyto-proSAAS spheres. Current studies involve attempts to create spheres *in vitro* (see for example (Sha et al., 2019)), though the insolubility of recombinant His-tagged proSAAS presents a difficulty in this regard.

A literature search to identify protein condensates similar to proSAAS spheres revealed that most aggresomes described to date are nuclear, much smaller (less than one micron), and heterogeneously shaped rather than spherical (reviewed in (Spannl et al., 2019; Wolozin and Ivanov, 2019)). Three nuclear protein condensates do produce membrane-less spherical particles. The first is the nuage protein DDX4, which forms micron-size spherical "organelles" (Nott et al., 2015). The second protein condensate is a portion of the RNA-binding protein matrin 3 (MATR3) (Gallego-Iradi et al., 2019), implicated in ALS. This protein contains an N-terminal domain involved in the phase separation of MATR3 droplets (Gallego-Iradi et al., 2019). A third nuclear protein which clearly forms distinct spheres is the renal protein nephrin (Pak et al., 2016). Interestingly, small nephrin spheres were able to fuse into larger structures, though again these were significantly smaller than the particles observed in our study. Although there is no apparent amino acid homology or composition similarity between DDX4 or MATR3 and proSAAS, a comparison between the intracellular motif of nephrin with the proSAAS sequence revealed the existence of weak homology [residue identity, 11/39 (28%); residue similarity 20/39 (51%)]. Of possible interest is the fact that this homology resides specifically within residues 74 to 106 of proSAAS, which corresponds to a predicted coiled-coil domain (residues 71-112). The contribution of coiled-coil domains to phase separation in the formation of membrane-less organelles such as P granules and promyelocytic leukemia nuclear bodies has been previously documented (reviewed in (Mitrea and Kriwacki, 2016)). ProSAAS also contains a predicted intrinsically disordered domain rich in prolines and alanines (residues 120-170); indeed, this region represents the most conserved portion of this protein (Jarvela et al., 2016; Kudo et al., 2009). The importance of disordered regions, including the contribution of prion-like domains, in phase transitions that lead to the formation of biomolecular condensates has been extensively reviewed (Banani et al., 2017; Gomes and Shorter, 2019). ProSAAS does not contain a prion-like domain, as predicted by the PLAAC algorithm (http://plaac.wi.mit.edu/; (Alberti et al., 2009)). We propose that the proSAAS coiled-coil and intrinsically disordered domains instead play important roles in the formation of cyto-proSAAS spheres as well as in the sphere fusion process.

Surprisingly, co-expression of cyto-proSAAS with TDP-43$^{216-414}$ radically altered the distribution of TDP-43 aggregates, as most cells then restricted their total TDP-43 fluorescence to the core of the proSAAS spheres. TDP-43 aggregates are predominantly cleared thorough proteasomal degradation following ubiquitination (Dong and Chen, 2018; Neumann et al., 2006), and we confirmed the presence of this modification on TDP-43 aggregates entering proSAAS spheres. Although the specific segment of TDP-43 we used in our studies is known to impair its autophagy (Cicardi et al., 2018), using a fluorescent autophagy (LC3) reporter we could rule out a role for cyto-proSAAS in TDP-43 autophagy. Taken together, these findings support the idea that aggregated, ubiquitinated TDP-43 bears a great affinity for cyto-proSAAS. While the specificity of proSAAS spheres for TDP-43$^{216-414}$ is clear (proSAAS spheres did not encapsulate fluorescent forms of HTT, tau, α-Syn, or other non-aggregating cytosolic proteins such as mCherry itself), the biochemical basis for this specificity is unknown. The glycine- and asparagine-rich prion-like domain within TDP-43$^{216-414}$ is thought to represent the major determinant for its aggregation (Johnson et al., 2009; Prasad et al., 2019; Schmidt et al., 2019). To our knowledge, there are no similar cytoplasmic TDP-43-containing particles which have been previously reported. Other TDP-43-containing granules reported in the literature to date are either nuclear; or can be labelled with antisera to RNA-binding proteins (reviewed in (Wolozin and Ivanov, 2019)). Structure-function experiments will be required to define the specific portions of proSAAS that underlie its affinity for TDP-43$^{216-414}$ and vice versa. TDP-43 was recently

reported to form spherical annuli inside the nucleus, which trap Hsp70 inside: https://www.biorxiv.org/content/10.1101/2020.03.28.985986v1.

Under what circumstances might proSAAS, a secretory chaperone, be physiologically present within the cytoplasm to be able to interact with TDP-43? Following ER stress, such as thapsigargin treatment, the secretory chaperone clusterin translocates to the cytoplasm and binds TDP-43$^{216-414}$ (Gregory et al., 2017; Nizard et al., 2007). ER reflux to the cytoplasm is a phenomenon also recognized in yeast (Igbaria et al., 2019). In our hands, expression of TDP-43$^{216-414}$ together with clusterin in the absence of stressors was itself sufficient to induce a large change in the distribution of both clusterin and TDP-43$^{216-414}$; and following the addition of ER stressors, we confirmed clusterin retrotranslocation (as indicated by co-localization with TDP-43$^{216-414}$). However, proSAAS co-localization with cytosolic TDP-43$^{216-414}$ was not apparent following similar treatment with stressors. We did observe increased co-localization of secretory proSAAS with cytoplasmic TDP-43$^{216-414}$ in a small subpopulation of highly differentiated Neuro2A cells present within our cultures, but efforts to transfect retinoic acid-differentiated Neuro2A cells to potentially expand this observation were not successful. Although further work is required, this limited evidence of proSAAS mobilization implies that cellular stress may alter proSAAS localization under select circumstances. Alternatively, secreted proSAAS may act extracellularly to bind toxic aggregates and reduce cell-to-cell propagation. Indeed TDP-43 has been shown to exhibit prion-like propagation (reviewed in (Prasad et al., 2019)); we speculate that secreted proSAAS may function to sequester secreted TDP-43 aggregates, reducing seeding. Interestingly, the TDP-43$^{219-414}$ form, which results from caspase cleavage (Zhang et al., 2007), has a higher potential for seeding aggregation as compared to other TDP-43 proteins ((Huang et al., 2014); see also (Nonaka and Hasegawa, 2019)). It should also be mentioned that TDP-43 deposition, while most commonly found in FTLD and ALS (reviewed in (Cook and Petrucelli, 2019)), also occurs in several other neurodegenerative diseases, including AD (reviewed in (Kovacs, 2019; Uchino et al., 2015)), hippocampal sclerosis (Kovacs et al., 2013), Lewy body disease (Nakashima-Yasuda et al., 2007)),and argyrophilic grain disease (Fujishiro et al., 2009); reviewed in (Arnold et al., 2013). Thus far no studies have investigated the potential colocalization of proSAAS with TDP-43 aggregates in tissues taken from patients with FTLD or ALS. ProSAAS has however been identified as a major proteomics hit in the CSF of FTLD patients (Davidsson et al., 2002); reviewed in (Hedl et al., 2019).

What are possible functional consequences of cyto-proSAAS sphere expression? Cyto-proSAAS clearly increases the half-life of TDP-43$^{219-414}$, most likely reflecting the sequestration of TDP-43$^{219-414}$ aggregates inside spheres. ProSAAS-induced changes in TDP-43$^{219-414}$ aggregate morphology may itself reduce the cytotoxic propensity of these aggregates (Bolognesi et al., 2019). Unfortunately, we could not assess the cytoprotective effects of cyto-proSAAS on TDP-43-mediated cytotoxicity in mammalian cells, as TDP-43 aggregates were not cytotoxic in our hands. In yeast cells, proSAAS, cyto-proSAAS and 7B2 partially rescued the growth impairment caused by expression of full-length TDP-43. Previous work on potentiated Hsp104 disaggregases showed that Hsp104-mediated rescue of aggregate toxicity in yeast models could be replicated in an animal nervous system (Jackrel et al., 2014). Other modifiers of TDP-43 toxicity in yeast have also translated to mouse models Elden (Elden et al., 2010) (Becker et al., 2017). Thus, our findings in yeast are highly promising in their suggestion of cytoprotective effects for proSAAS in higher eukaryotes.

In summary, we have identified a novel mechanism for aggregate protein sequestration via proSAAS sphere encapsulation. This action may explain the cytoprotective potency of

proSAAS in *in vitro* and *in vivo* experiments involving exposure to amyloid and synuclein oligomers (Hoshino et al., 2014; Jarvela et al., 2016). More speculatively, we suggest that expression of cyto-proSAAS spheres might represent a powerful approach to enhance TDP-43$^{216-414}$ sequestration in ALS and other neurodegenerative diseases.

Author Contributions: Conceptualization: JRP and IL. Investigation: JRP, TSJ, KC and EB. Methodology: JRP, TSJ, KC and EB. Software: JRP and TSJ. Formal analysis: JRP, EB and TSJ. Writing: original draft, JRP and IL. Writing: review and editing, TSJ, KC, EB, and IL. Project administration, supervision and funding acquisition: IL

Acknowledgments: We are grateful for research support from NIH grant AG 062222 to IL and support from "*Convocatorias de movilidad"* from University of Castilla-la Mancha (UCLM) to JRP. This work utilized an EM sample preparation instrument that was purchased with funding from a National Institutes of Health SIG grant (1S10RR26870-1). We are grateful for the assistance of Dr. Ru-ching Hsia of the Electron Microscopy Core Imaging Facility, Center for Innovative Biomedical Resources, University of Maryland-Baltimore. We acknowledge the use of the Confocal Microscopy Core Facility, University of Maryland-Baltimore. We thank Ms. Minerva Contreras for hippocampal cells, and our UMB colleagues Drs. Rizzo and Lipinski for various constructs. EB was supported by a Milton Safenowitz Post-Doctoral Fellowship from ALSA and by NIH grant F32NS108598. JS was supported by grants from ALSA, Target ALS, and The Robert Packard Center for ALS Research at Johns Hopkins.

Declaration of Interests: The authors declare no competing interests.

Further information and requests for resources and reagents: should be directed to and will be fulfilled by the Lead Contact, Iris Lindberg (ilindberg@som.umaryland.edu).

Materials Availability: All unique/stable reagents generated in this study are available from the Lead Contact without restriction.

MATERIALS AND METHODS

Cell culture

Neuro2A and HEK cells were obtained from ATCC (Manassas, VA) and grown in OptiMEM/DMEM and DMEM, respectively, both with 10% fetal bovine serum (FBS; Gemini Bio, West Sacramento, CA). Transfection of cells was carried out on 70-80% confluent cells in a 24-well plate fitted with poly-L-lysine-treated glass coverslips, using 0.5 - 1 μg of cDNA and a three-fold excess of FuGene (Promega, Madison, WI). Cells were harvested for immunocytochemistry 24 or 48 h after transfection. In order to induce differentiation of Neuro2A cells, the cells were maintained in OptiMEM/DMEM (InVitrogen/ThermoFisher, Carlsbad, CA) with 1% FBS for 2 days prior to transfection.

Hippocampal primary neurons obtained from E17 rat embryos were cultured as described previously (Frost et al., 2010) using digestion with 0.25% trypsin-EDTA and mechanical dissociation by gentle pipetting through a series of small-bore Pasteur pipettes. Filtered cells were resuspended in Neurobasal medium (InVitrogen) supplemented with 5% B27 supplement, 5% penicillin-streptomycin, and 2 mM L-GlutaMAX (all from InVitrogen), and then cultured on poly-L-lysine coated 12-mm coverslips at 37 °C and 5% CO_2 in a humidified atmosphere. Media were replaced every 3-4 days. Seven-day old primary hippocampal cells were transfected with

2 μg of cyto-proSAAS cDNA using Lipofectamine (Invitrogen). Cells were fixed, immunostained with FLAG and HA tag antisera, and imaged 24 h post-transfection. Between 5-10% of cells were transfected by this method.

Expression vectors

The majority of the constructs used for expressing aggregating proteins were obtained from Addgene (Watertown, MA). The Addgene catalog numbers are as follows: GFP-tagged TDP-43 constructs TDP-43$^{216-414}$, #28197; TDP-43$^{1-193}$ (#28202); TDP-43$^{1-273}$ (#28200); TDP-43 $^{86-414}$ (#28195) and TDP-43$^{170-414}$ (#28196), described in (Yang et al., 2010); HTT-Q74 (HTT exon 1 Q74, His- and HA-tagged, #40264, #40262); and GFP-HTT-Q74, in (Narain et al., 1999); EGFP-Tau, #46904, and EGFP-TauE14, #46907 (Hoover et al., 2010); EGFP-α-Syn, #40822 and EGFP-α-Syn-A53T, #40823 (Furlong et al., 2000); and pEGFP-N1-FUS/TLS-FLAGC, #60362 (Britton et al., 2014). HA-Ubiquitin-K48 (#17605)(Lim et al., 2005) and PABPC4-HA-FLAG, (#19882) (Landthaler et al., 2008) were also obtained from Addgene, while the LC3-mCherry construct was obtained from M.M. Lipinksi (U. Maryland-Baltimore; (Thayer et al., 2020)). The N-terminally FLAG-tagged mouse clusterin vector was obtained from Sino-Biological (#MG50485-NF).

A FLAG-tagged eukaryotic expression vector for murine proSAAS was constructed by Genscript (Piscataway, NJ) in pcDNA3.1(-) (hygromycin-resistant) by insertion of the nucleotide sequence GATTACAAGGATGACGACGATAAG, encoding the DYKDDDDK FLAG peptide, following the signal peptide. Signal-less cyto-proSAAS was created with a forward primer introducing a methionine amino terminal to the FLAG tag, and a reverse primer targeted to the c-terminus of proSAAS. This product was cloned into the *NheI* and *HindIII* sites of the pcDNA3.1(-) hygromycin resistance-encoding vector (Invitrogen). A signal-less form of 7B2 was constructed similarly. Lastly, the mCherry proSAAS fusion construct was made by N-terminal insertion of mCherry into the signal-less proSAAS construct. A cytoplasmic mCherry expression vector was obtained from Dr. Megan Rizzo (University of Maryland-Baltimore, MD). The mCherry-CART vector has been described (Blanco et al., 2015).

Confocal microscopy

For immunohistochemistry, cells were transfected in a 24-well plate on 12-mm coverslips and 24h later fixed in 4% PFA in PBS for 20 min. Cells were incubated for 30 min at room temperature in blocking buffer (PBS with 5% FBS, 0.5% Triton X-100 and 100 mM glycine). Antibodies against FLAG (Sigma-Aldrich, #F7425);); Rab7a (# NBP1-87174, Novus); HSP70 (#11660-T52; Sino Biological); TDP-43$^{216-414}$ (#NB11O-5537; Novus); and GFP (#GFP879484; Aves Labs, Inc); were used at a dilution of 1:1000 in blocking buffer and incubated for 30 min at room temperature. Anti-HA tag antiserum (Abcam, #130275) was incubated with cells overnight at a dilution of 1:200. After washing multiple times with PBS, cells were incubated with secondary fluorescent antibodies and Hoechst stain, both at a dilution of 1:5000. In some experiments, primary antibodies conjugated with fluorescent dyes were used; these were anti-FLAG (Alexa647; #637315; BioLegend), and anti-giantin (Alexa488; #908701; BioLegend), anti-LAMP-1 (Alexa488; #121607; BioLegend). The specificity of the proSAAS signal obtained with anti-FLAG antiserum was confirmed using IgG-purified antibody developed against the recombinant murine 21 kDa proSAAS protein (Hoshino et al., 2014). Morphological characterization of proSAAS spheres and quantitation of fluorescent signal and transfection efficiency was carried out using Fiji/ImageJ (Schindelin et al., 2012) and at least two 40x fields, obtained from three independent experiments, containing the same experimental conditions, were combined for statistical purposes.

In one set of experiments, sequential transfections were carried using HEK cells at 50% confluence in a 24-well dish in two steps: cells were first transfected with 1 μg of TDP-43$^{216-414}$ cDNA for 20 h using Fugene HD (Promega). After 5 washes with OptiMEM and a 3h preincubation with complete medium, cells were super-transfected with 1 μg of cyto-proSAAS for an additional 20 h. Cells were then washed, fixed and stained as described above. To study the nature of TDP-43$^{216-414}$ aggregates, Z-stacks stacks (0.2 μm intervals) of individual cells expressing TDP-43$^{216-414}$ aggregates, both within and outside cyto-proSAAS spheres, were obtained. For quantitative imaging, 12-bit images were taken, with care to avoid saturation of the GFP signal. The GFP signal within and outside the proSAAS spheres was quantified using 3D ImageJ Suite (Ollion et al., 2013). Images were first smoothed with a 1.5 pixel Gaussian blur and then segmented in the cyto-proSAAS channel with manual threshold adjustment to select only spheres. The TDP-43$^{216-414}$ channel was segmented with a threshold to include only aggregated GFP signal. Binary masks were generated using the segmented images and used to quantify the original GFP signal inside and outside the cyto-proSAAS sphere, using the Measure 3D and Quant 3D plugins.

Dynamic in vivo imaging

Live cell confocal microscopy was performed on a Nikon W1 spinning disk confocal system, on a Nikon Ti2 inverted microscope, with a Hamamatsu sCMOS camera, at the Confocal Microscopy Core Facility, University of Maryland Baltimore. Acquisition was controlled with Nikon Elements software. Cells were incubated at 37°C and under 5% CO_2 in Opti-MEM media during imaging. Cells were grown in high grid 500 35-mm plates (Ibidi; Fitchburg, WI) to 50% confluence, and double- (TDP-43$^{216-414}$ and cyto-proSAAS; equal ratio) or triple-transfected (TDP-43$^{216-414}$, cyto-proSAAS and Cherry cyto-proSAAS; 1, 1, and 0.2 μg respectively) 6 to 24 h prior to imaging GFP and mCherry fluorescence, as indicated in the figures. Live cell DIC and epi-fluorescent microscopy was performed on an Olympus VivaView. Cells were plated in 35-mm glass-bottomed dishes (MatTek; Ashland, MA) and transfected 18 h prior to the start of imaging. Multiple regions of cells were selected and imaged at 2 min intervals over a period of 6 h, using excitation/emission filter sets for GFP and RFP. Image analysis was performed with ImageJ.

Electron microscopy

HEK 293 cells were grown on 12-mm coverslips up to 70% confluence and transfected with empty vector, TDP-43$^{216-414}$ cDNA alone, or TDP-43$^{216-414}$ in combination with cyto-proSAAS cDNA. Twenty-four h after transfection, cells were fixed in a solution of 2% paraformaldehyde, 2.5% glutaraldehyde, in 0.1 M PIPES buffer (pH 7). After washing, cells were quenched with 50 mM glycine in 0.1 M PIPES buffer (pH 7) for 15 min and washed again with 0.1 M PIPES buffer, post-fixed in 1% (w/v) osmium tetroxide, 0.75% ferrocyanide in 0.1 M PIPES buffer for 60 min, washed with 0.1M PIPES, and stained with 1% (w/v) uranyl acetate in water for 30 min. After washing, specimens were dehydrated using serially graded ethanol solutions (30%, 50%, 70%, 90% and 100%) and infiltrated and embedded in Spurs resin (Electron Microscopy Sciences, Hatfield, PA) following the manufacturer's recommendations. Ultrathin sections (70 nm) were cut on a Leica UC6 ultramicrotome (Leica Microsystems, Inc., Bannockburn, IL), collected onto copper grids, and examined in a Tecnai T12 transmission electron microscope (Thermo Fisher (Formerly FEI. Co.), Hillsboro, OR) operated at 80 kEV. Digital images were acquired by using a bottom-mounted CCD camera (Advanced Microscopy Techniques, Corp, Woburn, MA) and AMT600 software.

Western blotting

Western blotting of HEK cell extracts was performed using 70- 80% confluent cells grown in 12-well plates. Cells were resuspended in 150 μl RIPA buffer (25 mM Tris pH 7–8, 150 mM NaCl, 0.1% SDS, 1% Triton X-100 and 0.5% sodium deoxycholate supplemented with protease inhibitors ("Complete"; Sigma-Aldrich, St. Louis, MO) and frozen prior to assay. Samples were thawed, boiled, electrophoresed on 15% acrylamide gels and blotted to nitrocellulose using a BioRad Turbo Blotter at 250 V for 10 min. Blots were blocked in 5% blotting grade milk in 0.05% Tween-20 and then incubated with primary antisera against GFP (1:1500; #879484; Aves Labs, Inc), anti-FLAG (Sigma-Aldrich, #F7425), anti-HA (Abcam, #ab130275) and anti-actin (# A2228; Sigma) in blotting buffer overnight at 4C. Secondary antisera were HRP-linked (Bio-Rad # s170-6516, 170-6615, and L005680A, respectively). The specificity of the proSAAS signal on the blot was confirmed using a different antibody developed against the recombinant proSAAS protein (Hoshino et al., 2014).

Cycloheximide experiments

HEK cells were plated in 12-well plates and transfected when 70-80% confluence was reached. Twenty μg/ml of cycloheximide (Sigma-Aldrich) was used to inhibit total protein synthesis 24 h after transfection. The cells were monitored for 6 h following addition of drug, a duration that resulted in 80% reduction of aggregates in cells transfected with TDP-43$^{216-414}$. Cells were lysed in Laemmli sample buffer at the times indicated in the Results and subjected to blotting using chicken antiserum against GFP (Aves Labs). Three independent experiments were used for quantification purposes. To investigate the cellular distribution of proteins following 6 h of cycloheximide treatment, an additional set of experiments was performed. To that end, cells were fixed and treated as previously indicated, immunostained using anti-FLAG antibody (Sigma-Aldrich, #F7425), and subjected to confocal imaging.

Induction of cell stress with thapsigargin

Induction of cell stress was accomplished using thapsigargin (Sigma-Aldrich). HEK and/or Neuro2A cells grown to 60-70% confluence in 24-well plates were transfected with 1 μg/well of total cDNA; 7 h later cells were treated with 12.5 nM thapsigargin in new complete medium overnight. Cells were then processed for immunostaining as described above. Quantification was performed using data obtained from the number of fields indicated in the figure legends.

Stress granule marker experiments

An HA- and FLAG-tagged construct encoding the stress granule marker polyadenylate binding protein 4 (PABPC4) (Landthaler et al., 2008) was transfected into HEK cells, either alone; together with either TDP-43$^{216-414}$ or cyto-proSAAS; or with both of the latter constructs, using FugeneHD. After 24 h of expression, the cells were fixed and stained with anti-HA antiserum (Abcam, #130275, 1:200) for PABPC4-HA-FLAG localization; and with anti-proSAAS IgG (1:2000; (4)) for cyto-proSAAS. Hoechst dye (1:5000) was used for nuclear staining.

Yeast cell screen for proSAAS/cyto-proSAAS rescue from TDP-43 cytotoxicity

Yeast experiments were performed using the BY4741*Δhsp104* strain. Expression of TDP-43 was induced from the pGAL1 promoter, which is maintained on a HIS3-selectable CEN plasmid (pEB413GAL_TDP-43). ProSAAS and 7B2 (and their signal-less forms) were expressed from pGAL1 on a separate URA3- selectable CEN plasmid (pEB416GAL). Prior to the yeast spotting assays and Western blotting, the yeast were cultured for 12 h at 30°C in pre-induction media containing 2% raffinose + synthetic-defined media lacking histidine and uracil (-his/ura).

For spotting assays, the samples were normalized to an OD_{600} of 2 and serially diluted five-fold per spot. Rescue of TDP-43 cytotoxicity was assessed after 48h of spot growth on 2% glucose or galactose -his/ura agar plates at 30°C. For Western blotting, the yeast were inoculated in liquid induction media containing 2% galactose -his/ura and grown for 6 h to induce protein expression. Normalized cell pellets were treated for 5 min with 0.1 M NaOH followed by resuspension in 1x SDS-PAGE sample buffer (100mM Tris-HCl pH 6.8, 4 mM EDTA, 4% SDS, 0.1% Bromophenol blue, 20% glycerol) + fungal protease inhibitor cocktail (Sigma, P8215) and then heated at 95°C for 10 min. Samples were electrophoresed on a 4-20% Criterion Precast Tris-HCl acrylamide gel (200V for 1 h) and transferred to a PVDF membrane (0.15 amp for 1 h). Blots were blocked with Li-COR Odyssey Blocking Buffer (PBS) and then incubated with primary antibodies: anti-FLAG (Sigma F1804, 1:1000 for proSAAS and 7B2), anti-TDP-43 (Proteintech 10782-2-AP, 1:1000), or anti-PGK1 (Invitrogen 459250, 1:1000). Blots were visualized after a 30 min incubation with secondary antibodies (Li-COR 680RD anti-rabbit 1:2500; Li-COR 800CW anti-mouse 1:5000).

Statistical analysis

We used GraphPad Prism 5.0 and 6.0 (GraphPad Software, La Jolla, USA) for statistical analyses and data presentation. Graphs represent means $\pm$ SD or SE, as indicated, with the number of replicates indicated in the Methods or Figure Legends. Student's unpaired two-tailed t-test was used for comparison of data obtained for fluorescence density measurements from at least three independent experiments, with $p<0.05$ considered significant.

Figure Legends

Figure 1. **Confocal images of HEK and Neuro2A cells 24 h after transfection with plasmid constructs that generate TDP-43 and HTT aggregates and the chaperones used in the present study.** Representative images of aggregates (*green*) observed after transfection of TDP-43$^{216-414}$ **(panel A),** HTT-Q74 **(panel B)**, and GFP-HTT-Q74 **(panel C)** in both HEK and Neuro2A cells. **Panels D-E** show the expression pattern of FLAG-tagged proSAAS **(panel D)** and FLAG-tagged clusterin **(panel E)** in HEK and Neuro2A cells, both shown in *red*. Images were taken at 40X 24h after transient transfection. Scale bar 10 μm. Magnified images on the right correspond to 10 μm. Arrow in **panel D** indicates the spherical structures in HEK cells transfected with proSAAS cDNA.

Figure 2. **ProSAAS and clusterin exert disparate effects on TDP-43$^{216-414}$ aggregation 24 h after expression in thapsigargin-treated Neuro2A cells. Panel A:** Cytoplasmic aggregates are present following co-expression of TDP-43$^{216-414}$ with proSAAS (*red*) (**upper row**) and clusterin (*red*) (**lower row**). **Panel B:** Thapsigargin treatment increases the co-localization of TDP-43$^{216-414}$ aggregates (*green*) with proSAAS in a subpopulation of Neuro2A cells which exhibit a differentiated morphology**.** Images were taken at 40X. Cells were transfected for 24 h following overnight treatment with thapsigargin (12.5 nM). Scale bar 10 μm. Magnified inserts correspond to 10 μm. Arrows indicate colocalization of proSAAS and TDP-43$^{216-414}$.

Figure 3. Cytoplasmic expression of proSAAS (cyto-proSAAS) results in sphere formation in Neuro2A cells; proSAAS spheres specifically encapsulate TDP-43$^{216-414}$ aggregates. Panel A: Representative confocal images of Neuro2A cells transfected with cyto-proSAAS cDNA for either 24 h (left) or 48 h (right) showing characteristic proSAAS-immunoreactive spheres (shown enlarged at right). **Panel B:** TDP-43$^{216-414}$ aggregates (**upper row**), but not HTT-Q74 aggregates (**middle row**) are found inside cyto-proSAAS spheres (*red*) when both are co-expressed in Neuro2A cells. The **lower row** shows the characteristic cytosolic fluorescence of the control protein mCherry (*red*), which is not accumulated within the cyto-proSAAS spheres *(green*) when both are co-expressed in Neuro2A cells. Images taken at 40X, 24 h after transfection. Scale bar, 10 μm. Magnified inserts correspond to 10 μm.

Figure 4. Structural information (confocal and electron-microscopy) depicting the redistribution of TDP-43$^{216-414}$ aggregates to cyto-proSAAS sphere cores. Panels A-D: Confocal images of HEK cells co-transfected with TDP-43$^{216-414}$ and cyto-proSAAS cDNAs**.** The great majority of transfected cells (93%) are similar to the cell shown in **Panel A**, with all aggregates present within the core of the cyto-proSAAS sphere. The remainder of the transfected cells (7%) exhibit the other types of aggregate distribution depicted in **Panels B-D**. In **Panel E,** a 3D visualization of the spherical cyto-proSAAS structures is shown. **Panel F** depicts electron microscopy images of HEK cells transfected only with TDP-43$^{216-414}$. The characteristic TDP-43$^{216-414}$ aggregates are indicated with arrows, and a magnified image is shown at right**. Panel G:** Electron microscopy images of HEK cells expressing TDP-43$^{216-414}$ and cyto-proSAAS, showing the characteristic dense spheres. Scale bars of 10 μm are indicated in the images. *Red*, cyto-proSAAS, *green*, GFP-TDP-43$^{216-414}$.

Figure 5. Co-expression of cyto-proSAAS, but not clusterin, increases the cellular half-life of TDP-43$^{216-414}$ upon cycloheximide treatment. **Panel A:** HEK cells transfected with cDNAs encoding TDP-43$^{216-414}$ alone, or in combination with cyto-proSAAS or clusterin, were monitored by Western blotting using an anti-GFP antibody (*left panels*). Quantitation is shown in the *right panel*; approximately 80% of TDP-43$^{216-414}$ disappears after 6 h of cycloheximide treatment when cells are co-transfected with either an empty vector or a clusterin-encoding vector; however, 43% remains in cells co-transfected with cyto-proSAAS (*, $p<0.05$). **Panel B:** Confocal images

taken prior to (0 h) and following (6 h) cycloheximide treatment confirm reduced cellular quantities of TDP-43$^{216-414}$ (*left*) and clusterin (*right*) following cycloheximide treatment; in contrast, TDP-43$^{216-414}$ fluorescence is retained within cyto-proSAAS spheres (*middle*). In *red*, the percentage of cells positive for anti-FLAG clusterin/proSAAS immunostaining (300 cells analyzed, from 4 different fields).

Figure 6. Cyto-proSAAS spheres associate with ubiquitinated TDP-43 and stress granules.

Panel 6A. Cyto-proSAAS is not itself ubiquitinated but is associated with highly K48-ubiquitinated TDP-43$^{216-414}$. Representative images of HEK cells expressing UbK48-HA with cyto-proSAAS **(top row)** or TDP-43$^{216-414}$ **(middle row)** or both **(bottom row)**. Immunostaining against FLAG and HA shows no colocalization of cyto-proSAAS and UbK48-HA **(top row)**. UbK48-HA is colocalized with TDP-43$^{216-414}$ (**middle row, notched arrowheads**). Increased colocalization of TDP-43$^{216-414}$ with UbK48-HA is observed in aggregates clustered proximal to the cyto-proSAAS spheres, suggesting preferential association (**bottom row, notched arrowheads**). Scale bar, 10 μm. Magnified inserts correspond to 10 υm.

Panel 6B. Expression of either TDP-43$^{216-414}$ or cyto-proSAAS induces stress granule formation; stress granules are proximal to cyto-proSAAS spheres**.** Representative images of HEK cells expressing PABPC4 alone **(top row)**; with TDP-43$^{216-414}$ **(middle row);** or with cyto-proSAAS **(bottom row).** Anti-HA staining shows diffuse PABPC4-HA-FLAG immunoreactivity when this marker is expressed alone **(top row)**, but punctate staining colocalized with TDP-43$^{216-414}$ in the presence of this protein (**middle row, notched arrowheads**). Immunostaining against HA and proSAAS reveals that PABPC4-HA-FLAG-positive puncta are proximal to cyto-proSAAS spheres **(bottom row, empty arrowhead)**. Scale bar, 10 μm. Magnified inserts correspond to 10 μm.

Figure 7. Functional effects of cyto-proSAAS expression: protection from aggregation and rescue from cytotoxicity.

Panel 7A. Expression of Cherry-cyto-proSAAS (*red*) generates dispersed cytosolic aggregates in Neuro2A cells (**top row**); co-transfection of Cherry-cyto-proSAAS with a five-fold excess of cyto-proSAAS (*green*) eliminates these dispersed aggregates and restores Cherry-tagged proSAAS fluorescence to the spheres (**bottom row**).

Panel 7B. ProSAAS and 7B2 rescue TDP-43 cytotoxicity in a yeast model**.** Serial-dilution spotting assay of yeast expressing TDP-43 and the indicated chaperone from a galactose-inducible promoter (**left side**). The empty vector is used as a negative control for chaperone activity and shows TDP-43-induced growth impairment on galactose. The left spotting plate shows equal spotting and no growth impairment of yeast on glucose media, which does not induce TDP-43 or chaperone expression. The right plate shows growth phenotypes upon induction with galactose. Spotting data are representative images of four independent trials. The expression of TDP-43 and chaperones was detected via Western blotting; PGK1 is used as a loading control (**right side**).

Supplemental Figure Legends

Supplemental Figure S1. The pattern of proSAAS expression in Neuro2A and HEK cells differs from that of the tagged secretory protein Cherry-CART and does not affect HTT-Q74 aggregation. Panel A: Immunostaining of proSAAS expressed for 48 h (*red*) reveals the appearance of spheres in 25% of HEK cells (**top**). Neuro2A cells rarely contained these spheres **(bottom). Panel B:** Immunostaining of proSAAS (red) 24 h after co-transfection with Cherry-CART (*green*) in both Neuro2A (**lower row**) and HEK cells (**upper row**) shows that each secretory protein is expressed in different granules with different diameters; colocalization was not detected (see magnified images). **Panel C:** Co-expression of HTT-Q74 with proSAAS (**upper row**) and clusterin (**lower row**) in HEK cells does not affect the distribution of HTT aggregates. Images were taken at 40X 24 h after transfection. Scale bar 10 μm. Magnified images on the right correspond to 10 μm.

Supplemental Figure S2. ProSAAS and clusterin produce disparate effects on TDP-43$^{216-414}$ aggregates in thapsigargin-treated HEK cells. Panel A: Co-expression of proSAAS (**upper row**) and clusterin (**lower row**) with TDP-43$^{216-414}$ in HEK cells, showing aggregate morphology. **Panel B:** Effect of 12.5 nM thapsigargin in HEK cells after expression of TDP-43$^{216-414}$ alone (**upper row**) or in combination with proSAAS (**middle row**) or clusterin (**lower row**). Images were taken at 40X. Cells were transfected for 24 h following overnight treatment with thapsigargin (12.5 nM). Scale bar 10 μm. Magnified images correspond to 10 μm. **Panels C** and **D** represent quantitation of 80 cells taken from 3 experiments; the mean $\pm$ SE is given. *, $p<0.05$.

Supplemental Figure S3. Overexpression of cyto-proSAAS results in the development of dense spheres. Panel A: Overexpressed cyto-proSAAS, which consists of mostly unprocessed 30 kDa proSAAS (as revealed by Western blotting), forms spheres that can be observed using light microscopy (**yellow arrows**). **Panel B:** After 48 h of expression the spheres grew in size, in both HEK cells (**panel B, left vs right sides**) and Neuro2A cells (not shown). **Panel C:** Expression of cyto-proSAAS in primary rat hippocampal cells results in the formation of spheres similar to those observed in Neuro2A and HEK cells. The border of the transfected cell is shown in white. **Panel D:** Delivery of FLAG-7B2 to the cytosol via signal peptide removal ("cyto-7B2") did not result in sphere formation, and cyto-7B2 immunoreactivity was both dispersed within the cytosol and concentrated near the cell membrane. Images were taken at 40X. Scale bar 10 μm.

Supplemental Figure S4. Cytoplasmic cyto-proSAAS spheres specifically encapsulate TDP-43$^{216-414}$ aggregates. Panel A: cyto-proSAAS expression alone. **Panel B**: TDP-43$^{216-414}$ aggregates**,** but not HTT-Q74 aggregates **(panel C)** nor GFP-HTT-Q74 aggregates **(panel D)** are found inside cyto-proSAAS spheres (*red*) in HEK cells. **Panel E** shows the characteristic cytosolic fluorescence of dispersed mCherry (*red*) aggregates that do not become accumulated within the cyto-proSAAS spheres (*green*). Images were taken 24 h after transfection at 40X. Scale bar 10 μm. Magnified images correspond to 10 μm.

Supplemental Figure S5. TDP-43 aggregates exhibit altered morphology once incorporated into the cyto-proSAAS spheres, which only capture those TDP-43 aggregates containing the prion-like domain. **Panel A:** Schematic view of the TDP-43 constructs used. TDP-43$^{86-414}$ (**panel B**) and TDP-43$^{170-414}$ (**panel C**) formed aggregates when expressed alone in HEK cells, and these were efficiently incorporated into cyto-proSAAS spheres when this protein was co-expressed. PrLD, prion-like domain; RRM, RNA binding domain; NES, nuclear export signal; NLS, nuclear localization signal. **Panel D-F**, Quantification of 3-dimensional Z-stacks for the size, dimensions,

and intensity of TDP-43$^{214-416}$ aggregates present either inside cyto-proSAAS spheres (*blue circles*), or outside cyto-proSAAS spheres (*red squares*). **Panel D:** Ratio of the total surface area of TDP-43$^{214-416}$ to the total volume of the same objects. **Panel E:** The mean pixel intensity for each group. **Panel F:** The total signal intensity of each group, determined by the sum of signal intensity of all pixels in that group. (n=12 cells, two-tailed paired t-test **p<0.05, **p<0.01, ***p<0.001*). **Panel G:** Transfection of TDP-43$^{216-414}$ cDNA, followed 24 h later by transfection of cyto-proSAAS cDNA, also results in the detection of TDP-43$^{216-414}$ aggregates inside sphere cores, supporting the idea that the TDP-43$^{216-414}$ core can be formed later than the spheres. Images taken at 40X. Scale bar 10 μm. Magnified inserts correspond to 10 μm.

Supplemental Figure S6. Various cellular markers of lysosomal (Lamp-1), Golgi (giantin), cell stress (HSP70) and autophagy (Cherry-LC3 co-expression) are not associated with cyto-proSAAS spheres. Panel A: Lack of immunostaining of Neuro2A cells with TDP-43 antibody (C-terminal; in *white*) after co-expression of cyto-proSAAS (*red*) and TDP-43$^{216-414}$ (*green*), shows that this antibody cannot penetrate inside the sphere, supporting core inaccessibility. **Arrows** indicate fluorescent but immunologically undetected TDP-43$^{216-414}$ aggregates inside spheres**.** **Panel B:** Cyto-proSAAS spheres are likely not destined for autophagy, as no fluorescent signal was observed inside cyto-proSAAS spheres following triple transfection of Cherry-LC3, cyto-proSAAS and TDP-43$^{216-414}$ cDNAs. **Panels C-D**: Lack of cyto-proSAAS sphere immunostaining with sera against Lamp-1 (**panel C**) giantin (**panel D**) and HSP70 (**panel E**).

Supplemental Figure S7: Dynamic imaging of non-aggregating Cherry-cyto-proSAAS demonstrates macro-scale fusion of large spheres, non-fusion interactions with TDP-43 aggregates, and extrusion of internal aggregates. Dynamic widefield microscopy of Cherry-cyto-proSAAS (*red*) and TDP-43$^{216-414}$ (*green*, with DIC) beginning 18 h post transfection at 2 min intervals for 5 h. See also ***Supplemental Movie 1***. **Panel A**: Images shown at 24 min intervals (top) depict generation of multiple spheres, some containing TDP-43$^{216-414}$ aggregates which condense and fuse into larger spheres. A subset of images (box) is shown below at 2 min intervals, which captures two large spheres condensing into one. **Panel B**: Rarely, internal TDP-43$^{216-414}$ was found to rapidly and wholly exit from the center of cyto-proSAAS spheres. Max projections are shown, but 3D analysis reveals TDP-43$^{216-424}$ to be entirely within the sphere at the beginning of the time course. Cyto-proSAAS, TDP-43$^{216-414}$ and Cherry-cyto-proSAAS were co-transfected in a ratio 1:1:0.2, as indicated in *Methods*. Scale bar, 10 μm. Magnified inserts correspond to 10 μm.

Supplemental Movie 1. Dynamic imaging of mCherry-cyto-proSAAS spheres shows macro-scale fusion of large spheres. Movie of Figure 7B. Dynamic widefield microscopy of mCherry-cyto-proSAAS (red) and GFP-TDP-43$^{216-414}$ (green), and DIC (grayscale) beginning 18 h post transfection of cyto-proSAAS, TDP-43$^{216-414}$ and mCherry-cyto-proSAAS (1:1:0.2 ratio). Each frame corresponds to 2 min in real time. The ImageJ plugin Linear Stack Alignment with SIFT was used to stabilize the movie around the transfected cell.

References

Abdi, F., Quinn, J.F., Jankovic, J., McIntosh, M., Leverenz, J.B., Peskind, E., Nixon, R., Nutt, J., Chung, K., Zabetian, C.*, et al.* (2006). Detection of biomarkers with a multiplex quantitative proteomic platform in cerebrospinal fluid of patients with neurodegenerative disorders. Journal of Alzheimer's disease : JAD *9*, 293-348.

Alberti, S., Halfmann, R., King, O., Kapila, A., and Lindquist, S. (2009). A systematic survey identifies prions and illuminates sequence features of prionogenic proteins. Cell *137*, 146-158.

Arnold, S.J., Dugger, B.N., and Beach, T.G. (2013). TDP-43 deposition in prospectively followed, cognitively normal elderly individuals: correlation with argyrophilic grains but not other concomitant pathologies. Acta neuropathologica *126*, 51-57.

Arrasate, M., and Finkbeiner, S. (2012). Protein aggregates in Huntington's disease. Experimental neurology *238*, 1-11.

Ayala, Y.M., Zago, P., D'Ambrogio, A., Xu, Y.F., Petrucelli, L., Buratti, E., and Baralle, F.E. (2008). Structural determinants of the cellular localization and shuttling of TDP-43. Journal of cell science *121*, 3778-3785.

Balchin, D., Hayer-Hartl, M., and Hartl, F.U. (2016). In vivo aspects of protein folding and quality control. Science (New York, N.Y.) *353*, aac4354.

Banani, S.F., Lee, H.O., Hyman, A.A., and Rosen, M.K. (2017). Biomolecular condensates: organizers of cellular biochemistry. Nature reviews. Molecular cell biology *18*, 285-298.

Becker, L.A., Huang, B., Bieri, G., Ma, R., Knowles, D.A., Jafar-Nejad, P., Messing, J., Kim, H.J., Soriano, A., Auburger, G.*, et al.* (2017). Therapeutic reduction of ataxin-2 extends lifespan and reduces pathology in TDP-43 mice. Nature *544*, 367-371.

Blanco, E.H., Ramos-Molina, B., and Lindberg, I. (2015). Revisiting PC1/3 Mutants: Dominant-Negative Effect of Endoplasmic Reticulum-Retained Mutants. Endocrinology *156*, 3625-3637.

Bobori, C., Theocharopoulou, G., and Vlamos, P. (2017). Molecular Chaperones in Neurodegenerative Diseases: A Short Review. Advances in experimental medicine and biology *987*, 219-231.

Bolognesi, B., Faure, A.J., Seuma, M., Schmiedel, J.M., Tartaglia, G.G., and Lehner, B. (2019). The mutational landscape of a prion-like domain. Nature communications *10*, 4162.

Britton, S., Dernoncourt, E., Delteil, C., Froment, C., Schiltz, O., Salles, B., Frit, P., and Calsou, P. (2014). DNA damage triggers SAF-A and RNA biogenesis factors exclusion from chromatin coupled to R-loops removal. Nucleic Acids Res *42*, 9047-9062.

Chiti, F., and Dobson, C.M. (2017). Protein Misfolding, Amyloid Formation, and Human Disease: A Summary of Progress Over the Last Decade. Annual review of biochemistry *86*, 27-68.

Choi, Y.S., Hou, S., Choe, L.H., and Lee, K.H. (2013). Targeted human cerebrospinal fluid proteomics for the validation of multiple Alzheimer's disease biomarker candidates. J Chromatogr B Analyt Technol Biomed Life Sci *930*, 129-135.

Cicardi, M.E., Cristofani, R., Rusmini, P., Meroni, M., Ferrari, V., Vezzoli, G., Tedesco, B., Piccolella, M., Messi, E., Galbiati, M.*, et al.* (2018). Tdp-25 Routing to Autophagy and Proteasome Ameliorates its Aggregation in Amyotrophic Lateral Sclerosis Target Cells. Scientific reports *8*, 12390.

Cook, C., and Petrucelli, L. (2019). Genetic Convergence Brings Clarity to the Enigmatic Red Line in ALS. Neuron *101*, 1057-1069.

Cushman, M., Johnson, B.S., King, O.D., Gitler, A.D., and Shorter, J. (2010). Prion-like disorders: blurring the divide between transmissibility and infectivity. Journal of cell science *123*, 1191-1201.

Davidsson, P., Sjogren, M., Andreasen, N., Lindbjer, M., Nilsson, C.L., Westman-Brinkmalm, A., and Blennow, K. (2002). Studies of the pathophysiological mechanisms in frontotemporal dementia by proteome analysis of CSF proteins. Brain research. Molecular brain research *109*, 128-133.

Dong, Y., and Chen, Y. (2018). The role of ubiquitinated TDP-43 in amyotrophic lateral sclerosis. Neuroimmunol Neuroinflammation *5*.
Elden, A.C., Kim, H.J., Hart, M.P., Chen-Plotkin, A.S., Johnson, B.S., Fang, X., Armakola, M., Geser, F., Greene, R., Lu, M.M.*, et al.* (2010). Ataxin-2 intermediate-length polyglutamine expansions are associated with increased risk for ALS. Nature *466*, 1069-1075.
Finehout, E.J., Franck, Z., Choe, L.H., Relkin, N., and Lee, K.H. (2007). Cerebrospinal fluid proteomic biomarkers for Alzheimer's disease. Ann Neurol *61*, 120-129.
Foster, E.M., Dangla-Valls, A., Lovestone, S., Ribe, E.M., and Buckley, N.J. (2019). Clusterin in Alzheimer's Disease: Mechanisms, Genetics, and Lessons From Other Pathologies. Frontiers in neuroscience *13*, 164.
Frost, N.A., Shroff, H., Kong, H., Betzig, E., and Blanpied, T.A. (2010). Single-molecule discrimination of discrete perisynaptic and distributed sites of actin filament assembly within dendritic spines. Neuron *67*, 86-99.
Fujishiro, H., Uchikado, H., Arai, T., Hasegawa, M., Akiyama, H., Yokota, O., Tsuchiya, K., Togo, T., Iseki, E., and Hirayasu, Y. (2009). Accumulation of phosphorylated TDP-43 in brains of patients with argyrophilic grain disease. Acta neuropathologica *117*, 151-158.
Furlong, R.A., Narain, Y., Rankin, J., Wyttenbach, A., and Rubinsztein, D.C. (2000). Alpha-synuclein overexpression promotes aggregation of mutant huntingtin. The Biochemical journal *346 Pt 3*, 577-581.
Gallego-Iradi, M.C., Strunk, H., Crown, A.M., Davila, R., Brown, H., Rodriguez-Lebron, E., and Borchelt, D.R. (2019). N-terminal sequences in matrin 3 mediate phase separation into droplet-like structures that recruit TDP43 variants lacking RNA binding elements. Laboratory investigation; a journal of technical methods and pathology *99*, 1030-1040.
Gasset-Rosa, F., Lu, S., Yu, H., Chen, C., Melamed, Z., Guo, L., Shorter, J., Da Cruz, S., and Cleveland, D.W. (2019). Cytoplasmic TDP-43 De-mixing Independent of Stress Granules Drives Inhibition of Nuclear Import, Loss of Nuclear TDP-43, and Cell Death. Neuron *102*, 339-357.e337.
Gomes, E., and Shorter, J. (2019). The molecular language of membraneless organelles. The Journal of biological chemistry *294*, 7115-7127.
Gregory, J.M., Whiten, D.R., Brown, R.A., Barros, T.P., Kumita, J.R., Yerbury, J.J., Satapathy, S., McDade, K., Smith, C., Luheshi, L.M.*, et al.* (2017). Clusterin protects neurons against intracellular proteotoxicity. Acta neuropathologica communications *5*, 81.
Hartl, F.U. (2017). Protein Misfolding Diseases. Annual review of biochemistry *86*, 21-26.
Hedl, T.J., San Gil, R., Cheng, F., Rayner, S.L., Davidson, J.M., De Luca, A., Villalva, M.D., Ecroyd, H., Walker, A.K., and Lee, A. (2019). Proteomics Approaches for Biomarker and Drug Target Discovery in ALS and FTD. Frontiers in neuroscience *13*, 548.
Helwig, M., Hoshino, A., Berridge, C., Lee, S.N., Lorenzen, N., Otzen, D.E., Eriksen, J.L., and Lindberg, I. (2013). The neuroendocrine protein 7B2 suppresses the aggregation of neurodegenerative disease-related proteins. The Journal of biological chemistry *288*, 1114-1124.
Holtta, M., Minthon, L., Hansson, O., Holmen-Larsson, J., Pike, I., Ward, M., Kuhn, K., Ruetschi, U., Zetterberg, H., Blennow, K.*, et al.* (2015). An integrated workflow for multiplex CSF proteomics and peptidomics-identification of candidate cerebrospinal fluid biomarkers of Alzheimer's disease. Journal of proteome research *14*, 654-663.
Hoover, B.R., Reed, M.N., Su, J., Penrod, R.D., Kotilinek, L.A., Grant, M.K., Pitstick, R., Carlson, G.A., Lanier, L.M., Yuan, L.L.*, et al.* (2010). Tau mislocalization to dendritic spines mediates synaptic dysfunction independently of neurodegeneration. Neuron *68*, 1067-1081.
Hoshino, A., Helwig, M., Razaei, S., Berridge, C., Eriksen, J., and Lindberg, I. (2014). A novel function for proSAAS as an amyloid anti-aggregant in Alzheimer's disease. Journal of neurochemistry *128*, 419-430.
Huang, C.C., Bose, J.K., Majumder, P., Lee, K.H., Huang, J.T., Huang, J.K., and Shen, C.K. (2014). Metabolism and mis-metabolism of the neuropathological signature protein TDP-43. Journal of cell science *127*, 3024-3038.

Igbaria, A., Merksamer, P.I., Trusina, A., Tilahun, F., Johnson, J.R., Brandman, O., Krogan, N.J., Weissman, J.S., and Papa, F.R. (2019). Chaperone-mediated reflux of secretory proteins to the cytosol during endoplasmic reticulum stress. Proceedings of the National Academy of Sciences of the United States of America *116*, 11291-11298.
Jackrel, M.E., DeSantis, M.E., Martinez, B.A., Castellano, L.M., Stewart, R.M., Caldwell, K.A., Caldwell, G.A., and Shorter, J. (2014). Potentiated Hsp104 variants antagonize diverse proteotoxic misfolding events. Cell *156*, 170-182.
Jahn, H., Wittke, S., Zurbig, P., Raedler, T.J., Arlt, S., Kellmann, M., Mullen, W., Eichenlaub, M., Mischak, H., and Wiedemann, K. (2011). Peptide fingerprinting of Alzheimer's disease in cerebrospinal fluid: identification and prospective evaluation of new synaptic biomarkers. PloS one *6*, e26540.
Jarvela, T.S., Lam, H.A., Helwig, M., Lorenzen, N., Otzen, D.E., McLean, P.J., Maidment, N.T., and Lindberg, I. (2016). The neural chaperone proSAAS blocks alpha-synuclein fibrillation and neurotoxicity. Proceedings of the National Academy of Sciences of the United States of America *113*, E4708-4715.
Johnson, B.S., Snead, D., Lee, J.J., McCaffery, J.M., Shorter, J., and Gitler, A.D. (2009). TDP-43 is intrinsically aggregation-prone, and amyotrophic lateral sclerosis-linked mutations accelerate aggregation and increase toxicity. The Journal of biological chemistry *284*, 20329-20339.
Kikuchi, K., Arawaka, S., Koyama, S., Kimura, H., Ren, C.H., Wada, M., Kawanami, T., Kurita, K., Daimon, M., Kawakatsu, S*., et al.* (2003). An N-terminal fragment of ProSAAS (a granin-like neuroendocrine peptide precursor) is associated with tau inclusions in Pick's disease. Biochemical and biophysical research communications *308*, 646-654.
Klaips, C.L., Jayaraj, G.G., and Hartl, F.U. (2018). Pathways of cellular proteostasis in aging and disease. The Journal of cell biology *217*, 51-63.
Kovacs, G.G. (2019). Molecular pathology of neurodegenerative diseases: principles and practice. Journal of clinical pathology *72*, 725-735.
Kovacs, G.G., Milenkovic, I., Wohrer, A., Hoftberger, R., Gelpi, E., Haberler, C., Honigschnabl, S., Reiner-Concin, A., Heinzl, H., Jungwirth, S*., et al.* (2013). Non-Alzheimer neurodegenerative pathologies and their combinations are more frequent than commonly believed in the elderly brain: a community-based autopsy series. Acta neuropathologica *126*, 365-384.
Kudo, H., Liu, J., Jansen, E.J., Ozawa, A., Panula, P., Martens, G.J., and Lindberg, I. (2009). Identification of proSAAS homologs in lower vertebrates: conservation of hydrophobic helices and convertase-inhibiting sequences. Endocrinology *150*, 1393-1399.
Landthaler, M., Gaidatzis, D., Rothballer, A., Chen, P.Y., Soll, S.J., Dinic, L., Ojo, T., Hafner, M., Zavolan, M., and Tuschl, T. (2008). Molecular characterization of human Argonaute-containing ribonucleoprotein complexes and their bound target mRNAs. Rna *14*, 2580-2596.
Lee, S.N., and Lindberg, I. (2008). 7B2 prevents unfolding and aggregation of prohormone convertase 2. Endocrinology *149*, 4116-4127.
Lim, K.L., Chew, K.C., Tan, J.M., Wang, C., Chung, K.K., Zhang, Y., Tanaka, Y., Smith, W., Engelender, S., Ross, C.A*., et al.* (2005). Parkin mediates nonclassical, proteasomal-independent ubiquitination of synphilin-1: implications for Lewy body formation. J Neurosci *25*, 2002-2009.
Mackenzie, I.R., Rademakers, R., and Neumann, M. (2010). TDP-43 and FUS in amyotrophic lateral sclerosis and frontotemporal dementia. The Lancet. Neurology *9*, 995-1007.
Mathys, H., Davila-Velderrain, J., Peng, Z., Gao, F., Mohammadi, S., Young, J.Z., Menon, M., He, L., Abdurrob, F., Jiang, X*., et al.* (2019). Single-cell transcriptomic analysis of Alzheimer's disease. Nature *570*, 332-337.
Mitrea, D.M., and Kriwacki, R.W. (2016). Phase separation in biology; functional organization of a higher order. Cell communication and signaling : CCS *14*, 1.
Nakashima-Yasuda, H., Uryu, K., Robinson, J., Xie, S.X., Hurtig, H., Duda, J.E., Arnold, S.E., Siderowf, A., Grossman, M., Leverenz, J.B*., et al.* (2007). Co-morbidity of TDP-43 proteinopathy in Lewy body related diseases. Acta neuropathologica *114*, 221-229.

Narain, Y., Wyttenbach, A., Rankin, J., Furlong, R.A., and Rubinsztein, D.C. (1999). A molecular investigation of true dominance in Huntington's disease. Journal of medical genetics *36*, 739-746.
Neumann, M., Sampathu, D.M., Kwong, L.K., Truax, A.C., Micsenyi, M.C., Chou, T.T., Bruce, J., Schuck, T., Grossman, M., Clark, C.M.*, et al.* (2006). Ubiquitinated TDP-43 in frontotemporal lobar degeneration and amyotrophic lateral sclerosis. Science (New York, N.Y.) *314*, 130-133.
Nizard, P., Tetley, S., Le Drean, Y., Watrin, T., Le Goff, P., Wilson, M.R., and Michel, D. (2007). Stress-induced retrotranslocation of clusterin/ApoJ into the cytosol. Traffic (Copenhagen, Denmark) *8*, 554-565.
Nonaka, T., and Hasegawa, M. (2019). Prion-like properties of assembled TDP-43. Current opinion in neurobiology *61*, 23-28.
Nott, T.J., Petsalaki, E., Farber, P., Jervis, D., Fussner, E., Plochowietz, A., Craggs, T.D., Bazett-Jones, D.P., Pawson, T., Forman-Kay, J.D.*, et al.* (2015). Phase transition of a disordered nuage protein generates environmentally responsive membraneless organelles. Molecular cell *57*, 936-947.
Ollion, J., Cochennec, J., Loll, F., Escude, C., and Boudier, T. (2013). TANGO: a generic tool for high-throughput 3D image analysis for studying nuclear organization. Bioinformatics (Oxford, England) *29*, 1840-1841.
Pak, C.W., Kosno, M., Holehouse, A.S., Padrick, S.B., Mittal, A., Ali, R., Yunus, A.A., Liu, D.R., Pappu, R.V., and Rosen, M.K. (2016). Sequence Determinants of Intracellular Phase Separation by Complex Coacervation of a Disordered Protein. Molecular cell *63*, 72-85.
Peinado, J.R., Sami, F., Rajpurohit, N., and Lindberg, I. (2013). Blockade of islet amyloid polypeptide fibrillation and cytotoxicity by the secretory chaperones 7B2 and proSAAS. FEBS letters *587*, 3406-3411.
Prasad, A., Bharathi, V., Sivalingam, V., Girdhar, A., and Patel, B.K. (2019). Molecular Mechanisms of TDP-43 Misfolding and Pathology in Amyotrophic Lateral Sclerosis. Frontiers in molecular neuroscience *12*, 25.
Schindelin, J., Arganda-Carreras, I., Frise, E., Kaynig, V., Longair, M., Pietzsch, T., Preibisch, S., Rueden, C., Saalfeld, S., Schmid, B.*, et al.* (2012). Fiji: an open-source platform for biological-image analysis. Nature methods *9*, 676-682.
Schmidt, H.B., Barreau, A., and Rohatgi, R. (2019). Phase separation-deficient TDP43 remains functional in splicing. Nature communications *10*, 4890.
Sha, E., Nakamura, M., Ankai, K., Yamamoto, Y.Y., Oka, T., and Yohda, M. (2019). Functional and structural characterization of HspB1/Hsp27 from Chinese hamster ovary cells. FEBS open bio *9*, 1826-1834.
Spannl, S., Tereshchenko, M., Mastromarco, G.J., Ihn, S.J., and Lee, H.O. (2019). Biomolecular condensates in neurodegeneration and cancer. Traffic (Copenhagen, Denmark) *20*, 890-911.
Spellman, D.S., Wildsmith, K.R., Honigberg, L.A., Tuefferd, M., Baker, D., Raghavan, N., Nairn, A.C., Croteau, P., Schirm, M., Allard, R.*, et al.* (2015). Development and evaluation of a multiplexed mass spectrometry based assay for measuring candidate peptide biomarkers in Alzheimer's Disease Neuroimaging Initiative (ADNI) CSF. Proteomics. Clinical applications *9*, 715-731.
Thayer, J.A., Awad, O., Hegdekar, N., Sarkar, C., Tesfay, H., Burt, C., Zeng, X., Feldman, R.A., and Lipinski, M.M. (2020). The PARK10 gene USP24 is a negative regulator of autophagy and ULK1 protein stability. Autophagy *16*, 140-153.
Uchino, A., Takao, M., Hatsuta, H., Sumikura, H., Nakano, Y., Nogami, A., Saito, Y., Arai, T., Nishiyama, K., and Murayama, S. (2015). Incidence and extent of TDP-43 accumulation in aging human brain. Acta neuropathologica communications *3*, 35.
Valastyan, J.S., and Lindquist, S. (2014). Mechanisms of protein-folding diseases at a glance. Disease models & mechanisms *7*, 9-14.
Wada, M., Ren, C.H., Koyama, S., Arawaka, S., Kawakatsu, S., Kimura, H., Nagasawa, H., Kawanami, T., Kurita, K., Daimon, M.*, et al.* (2004). A human granin-like neuroendocrine peptide

precursor (proSAAS) immunoreactivity in tau inclusions of Alzheimer's disease and parkinsonism-dementia complex on Guam. Neurosci Lett *356*, 49-52.
Wang, J., Cunningham, R., Zetterberg, H., Asthana, S., Carlsson, C., Okonkwo, O., and Li, L. (2016). Label-free quantitative comparison of cerebrospinal fluid glycoproteins and endogenous peptides in subjects with Alzheimer's disease, mild cognitive impairment, and healthy individuals. Proteomics. Clinical applications *10*, 1225-1241.
Wardman, J.H., and Fricker, L.D. (2014). ProSAAS-derived peptides are differentially processed and sorted in mouse brain and AtT-20 cells. PloS one *9*, e104232.
Webster, J.M., Darling, A.L., Uversky, V.N., and Blair, L.J. (2019). Small Heat Shock Proteins, Big Impact on Protein Aggregation in Neurodegenerative Disease. Frontiers in pharmacology *10*, 1047.
Whiten, D.R., Cox, D., Horrocks, M.H., Taylor, C.G., De, S., Flagmeier, P., Tosatto, L., Kumita, J.R., Ecroyd, H., Dobson, C.M.*, et al.* (2018). Single-Molecule Characterization of the Interactions between Extracellular Chaperones and Toxic alpha-Synuclein Oligomers. Cell reports *23*, 3492-3500.
Wolozin, B., and Ivanov, P. (2019). Stress granules and neurodegeneration. Nature reviews. Neuroscience *20*, 649-666.
Yang, C., Tan, W., Whittle, C., Qiu, L., Cao, L., Akbarian, S., and Xu, Z. (2010). The C-terminal TDP-43 fragments have a high aggregation propensity and harm neurons by a dominant-negative mechanism. PloS one *5*, e15878.
Zhang, Y.J., Xu, Y.F., Dickey, C.A., Buratti, E., Baralle, F., Bailey, R., Pickering-Brown, S., Dickson, D., and Petrucelli, L. (2007). Progranulin mediates caspase-dependent cleavage of TAR DNA binding protein-43. J Neurosci *27*, 10530-10534.

Figure 1

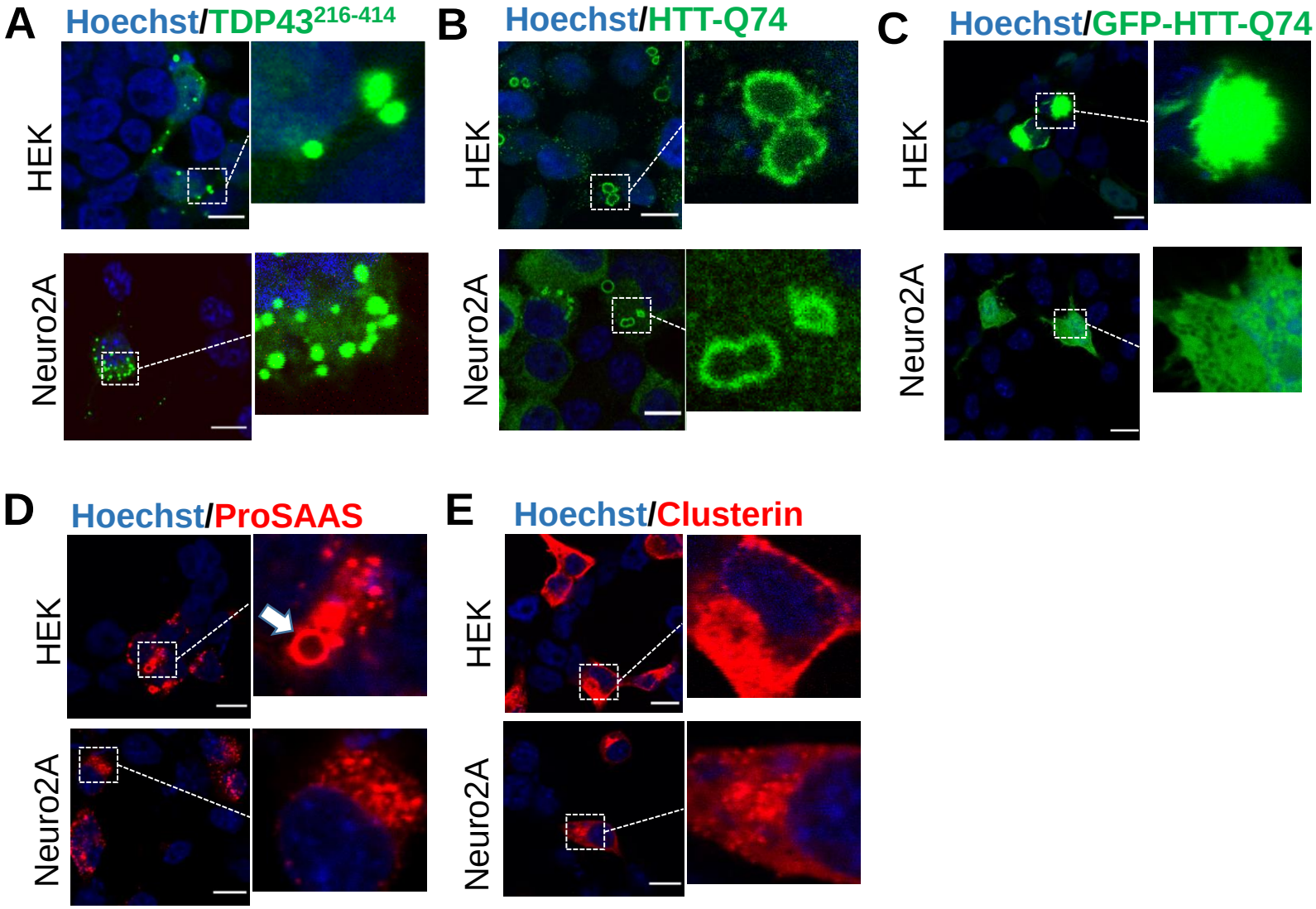
A
Hoechst/TDP43216-414
HEK
Neuro2A
B
Hoechst/HTT-Q74
HEK
Neuro2A
C
Hoechst/GFP-HTT-Q74
HEK
Neuro2A
D
Hoechst/ProSAAS
HEK
Neuro2A
E
Hoechst/Clusterin
HEK
Neuro2A

Figure 2

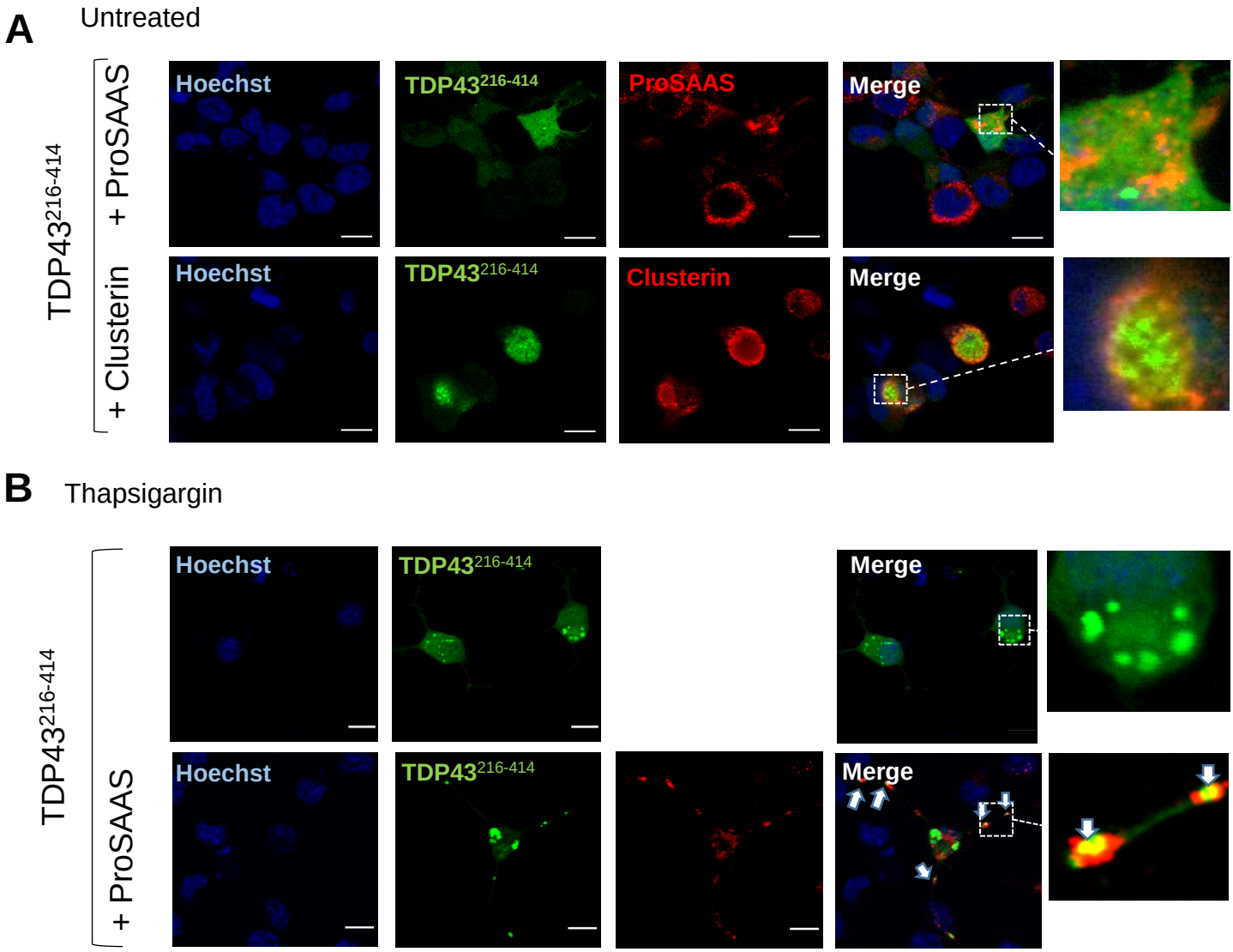
A
Untreated
TDP43216-414
+ ProSAAS
+ Clusterin
Hoechst
TDP43216-414
ProSAAS
Merge
Hoechst
TDP43216-414
Clusterin
Merge
B
Thapsigargin
TDP43216-414
+ ProSAAS
Hoechst
TDP43216-414
Merge
Hoechst
TDP43216-414
Merge

Figure 3

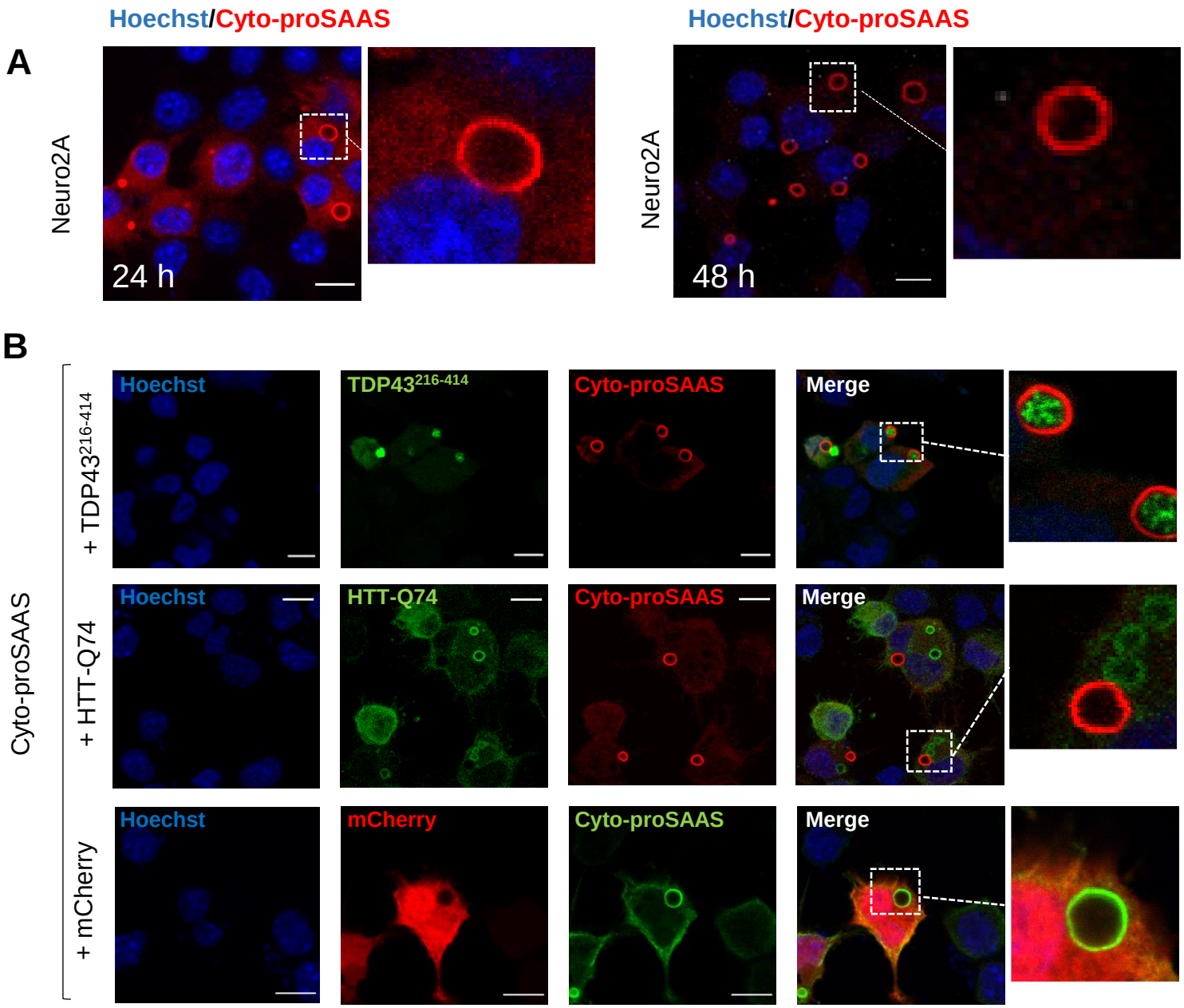
A
Hoechst/Cyto-proSAAS
Neuro2A
24 h
Hoechst/Cyto-proSAAS
Neuro2A
48 h
B
Cyto-proSAAS
+ TDP43216-414
Hoechst
TDP43216-414
Cyto-proSAAS
Merge
+ HTT-Q74
Hoechst
HTT-Q74
Cyto-proSAAS
Merge
+ mCherry
Hoechst
mCherry
Cyto-proSAAS
Merge

Figure 4

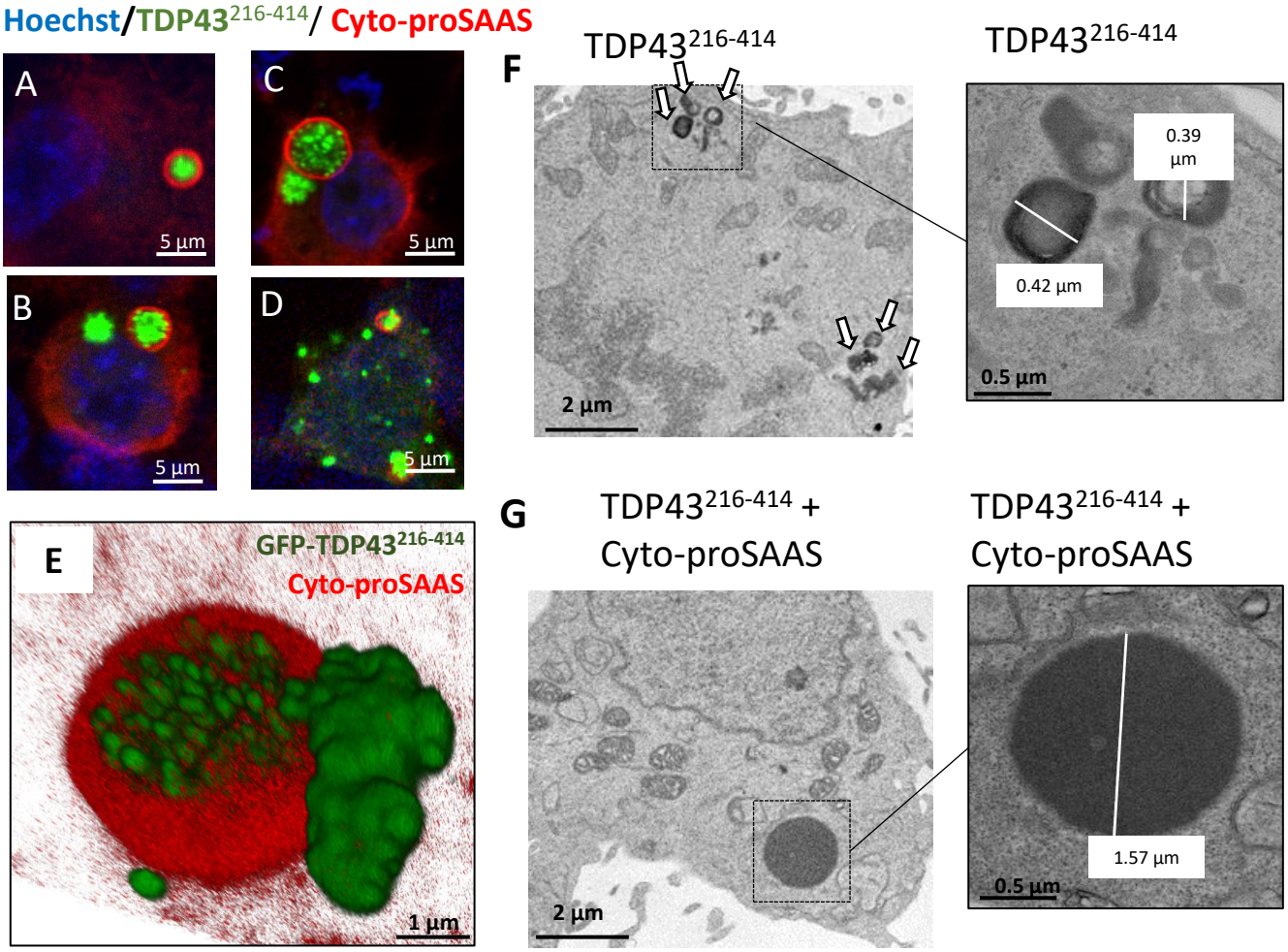
Hoechst/TDP43216-414/ Cyto-proSAAS
A
B
C
D
5 µm
E
GFP-TDP43216-414
Cyto-proSAAS
1 µm
F
TDP43216-414
2 µm
TDP43216-414
0.39 µm
0.42 µm
0.5 µm
G
TDP43216-414 + Cyto-proSAAS
2 µm
TDP43216-414 + Cyto-proSAAS
1.57 µm
0.5 µm

Figure 5

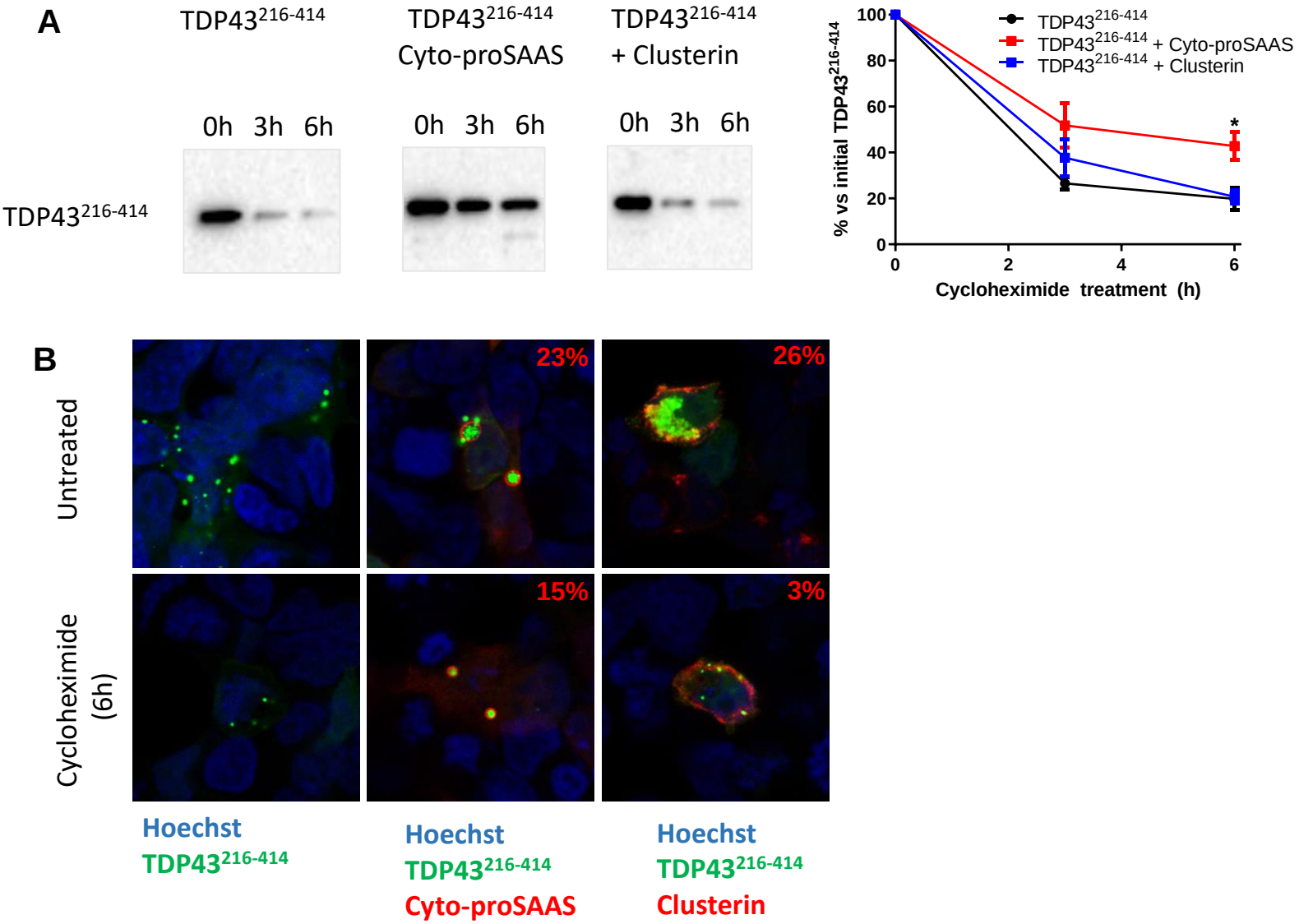
A
TDP43216-414
TDP43216-414 Cyto-proSAAS
TDP43216-414 + Clusterin
0h 3h 6h
0h 3h 6h
0h 3h 6h
TDP43216-414
100
80
60
40
20
0
% vs initial TDP43216-414
0
2
4
6
Cycloheximide treatment (h)
TDP43216-414
TDP43216-414 + Cyto-proSAAS
TDP43216-414 + Clusterin
*
B
Untreated
Cycloheximide (6h)
23%
26%
15%
3%
Hoechst
TDP43216-414
Hoechst
TDP43216-414
Cyto-proSAAS
Hoechst
TDP43216-414
Clusterin

Figure 6

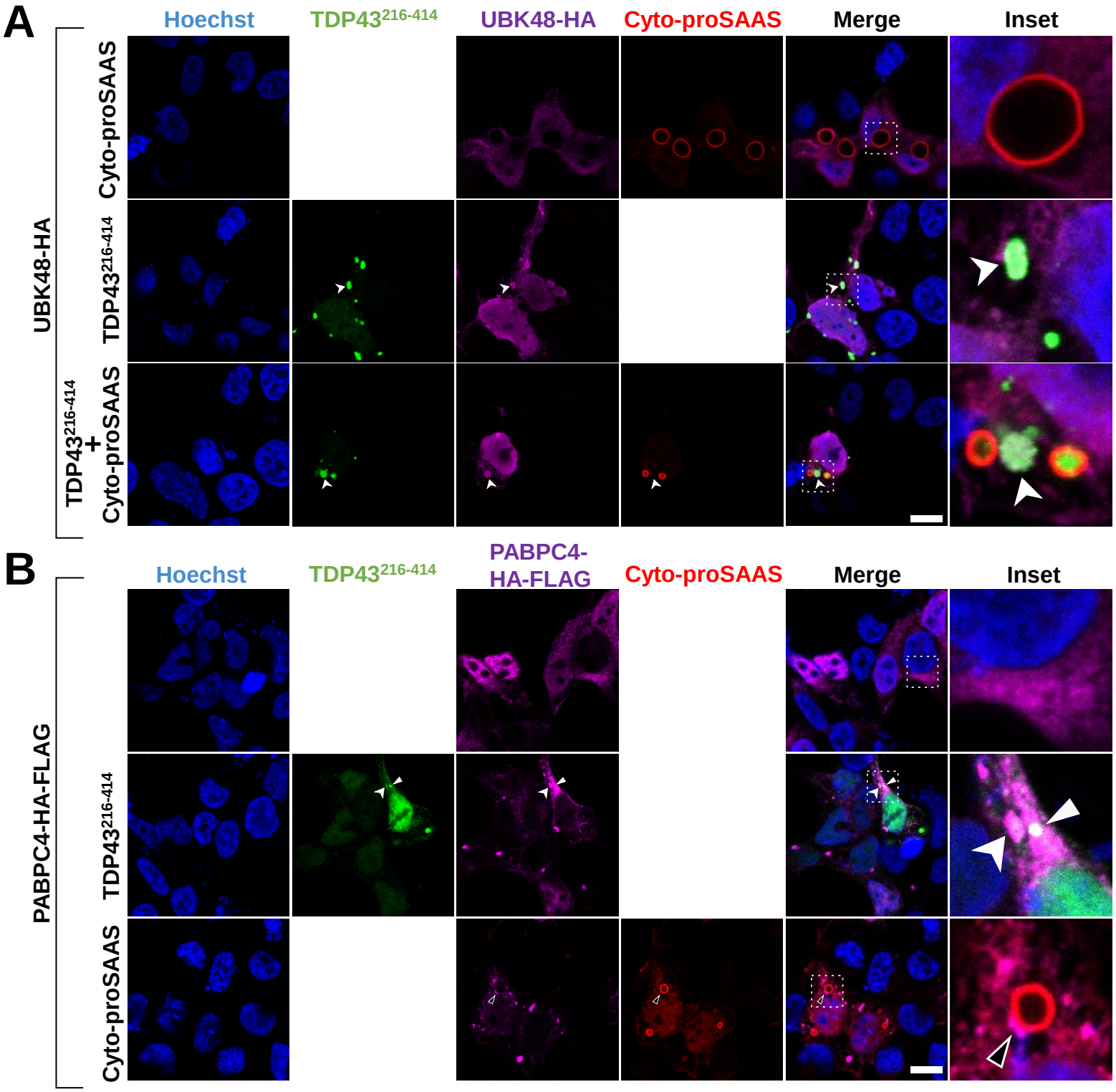
A
Hoechst
TDP43216-414
UBK48-HA
Cyto-proSAAS
Merge
Inset
UBK48-HA
Cyto-proSAAS
TDP43216-414
TDP43216-414 + Cyto-proSAAS
B
Hoechst
TDP43216-414
PABPC4-HA-FLAG
Cyto-proSAAS
Merge
Inset
PABPC4-HA-FLAG
TDP43216-414
Cyto-proSAAS

Figure 7

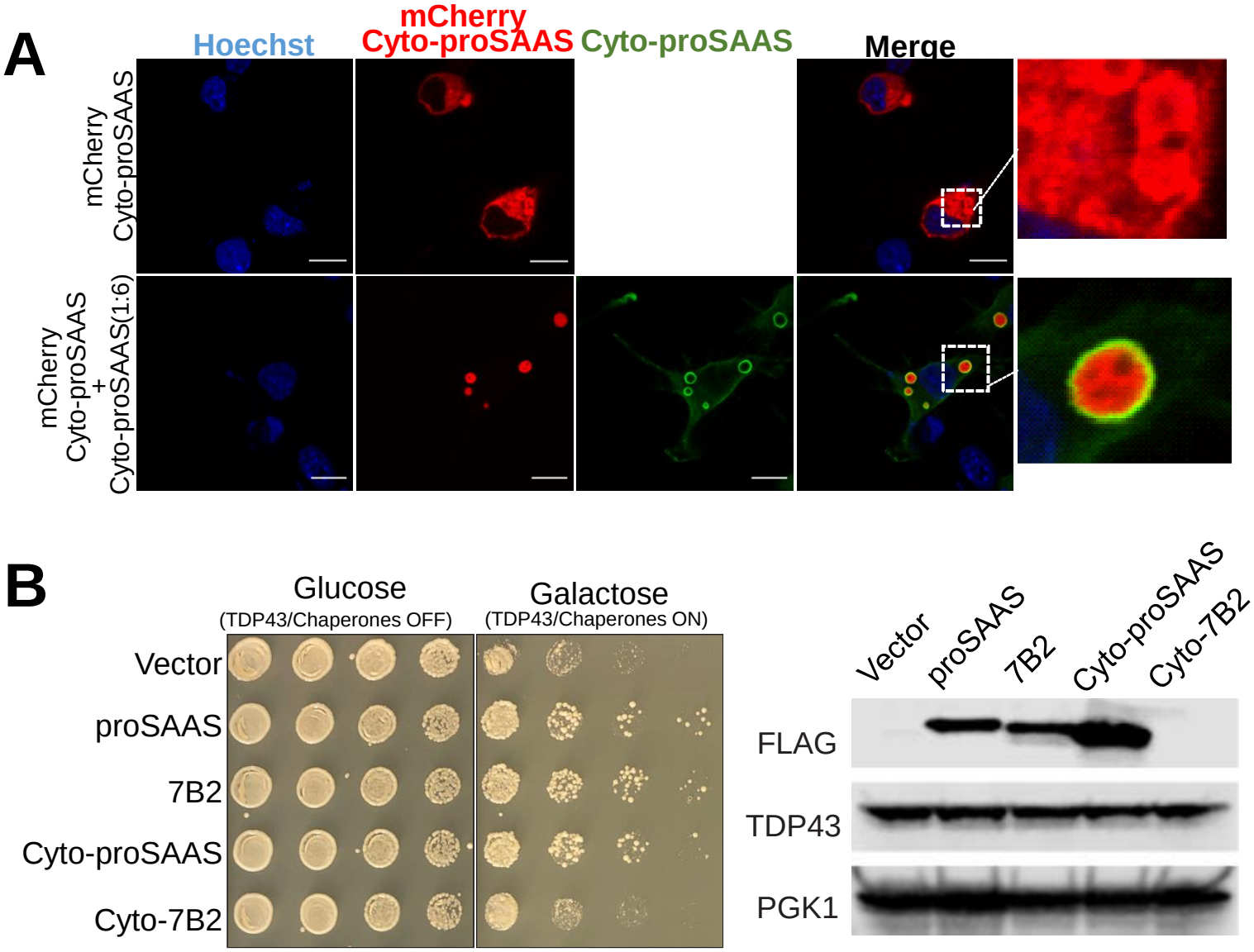
A
Hoechst
mCherry
Cyto-proSAAS
Cyto-proSAAS
Merge
mCherry
Cyto-proSAAS
mCherry
Cyto-proSAAS
+
Cyto-proSAAS(1:6)
B
Glucose
(TDP43/Chaperones OFF)
Galactose
(TDP43/Chaperones ON)
Vector
proSAAS
7B2
Cyto-proSAAS
Cyto-7B2
Vector
proSAAS
7B2
Cyto-proSAAS
Cyto-7B2
FLAG
TDP43
PGK1

Figure S1

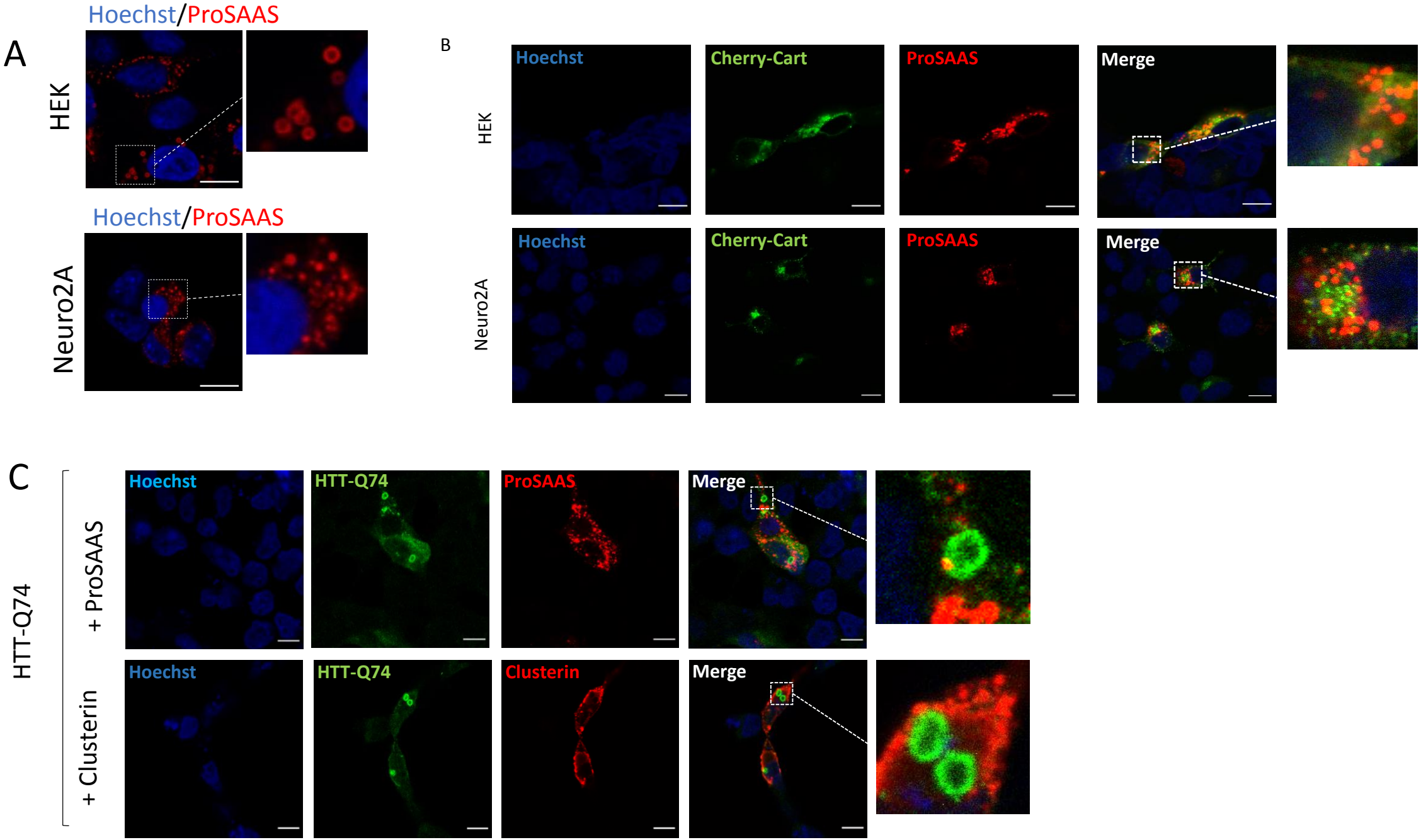
A
Hoechst/ProSAAS
HEK
Hoechst/ProSAAS
Neuro2A
B
HEK
Hoechst
Cherry-Cart
ProSAAS
Merge
Neuro2A
Hoechst
Cherry-Cart
ProSAAS
Merge
C
HTT-Q74
+ ProSAAS
Hoechst
HTT-Q74
ProSAAS
Merge
+ Clusterin
Hoechst
HTT-Q74
Clusterin
Merge

Figure S2

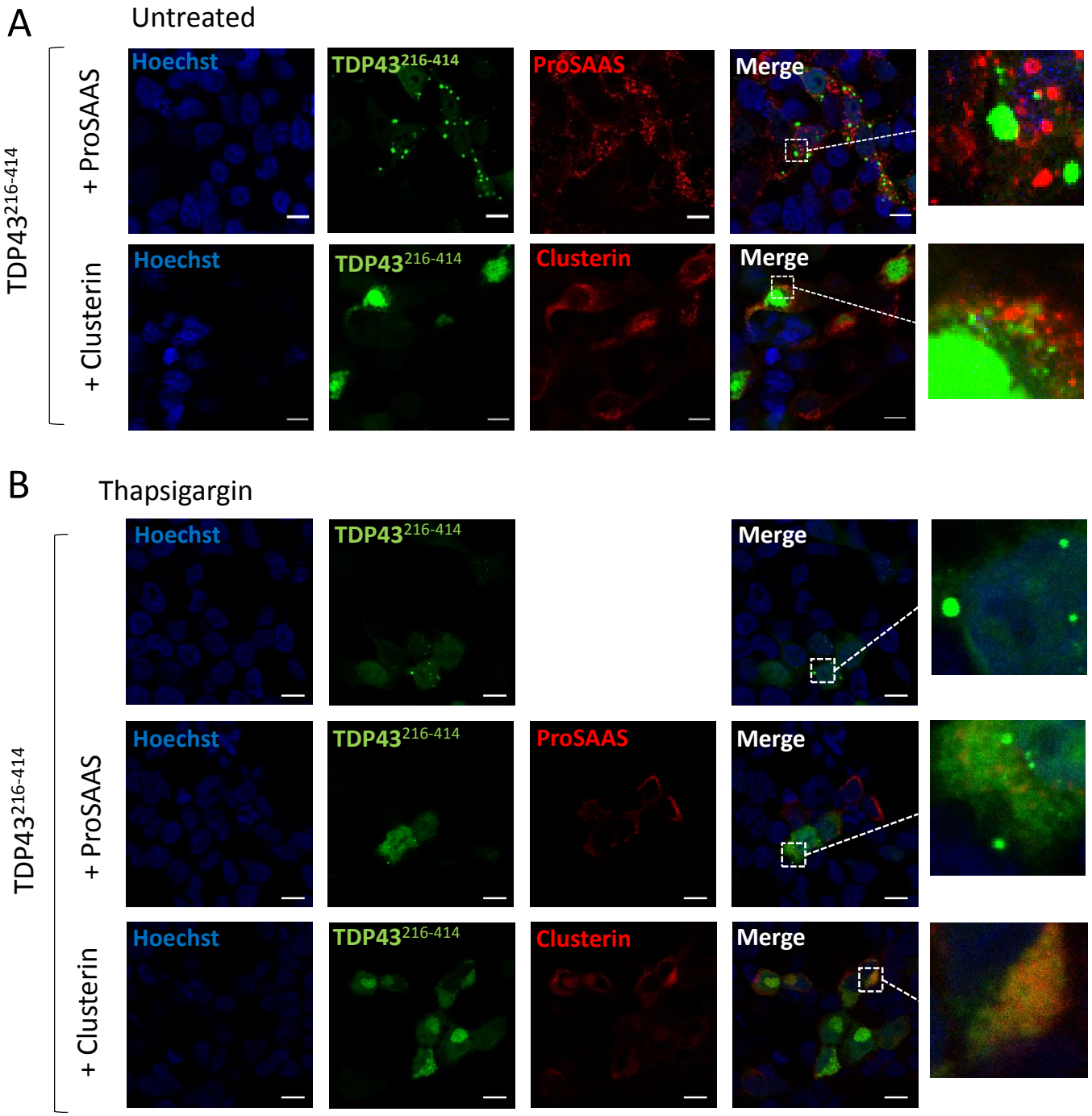
A
Untreated
TDP43216-414
+ ProSAAS
+ Clusterin
Hoechst
TDP43216-414
ProSAAS
Clusterin
Merge
B
Thapsigargin

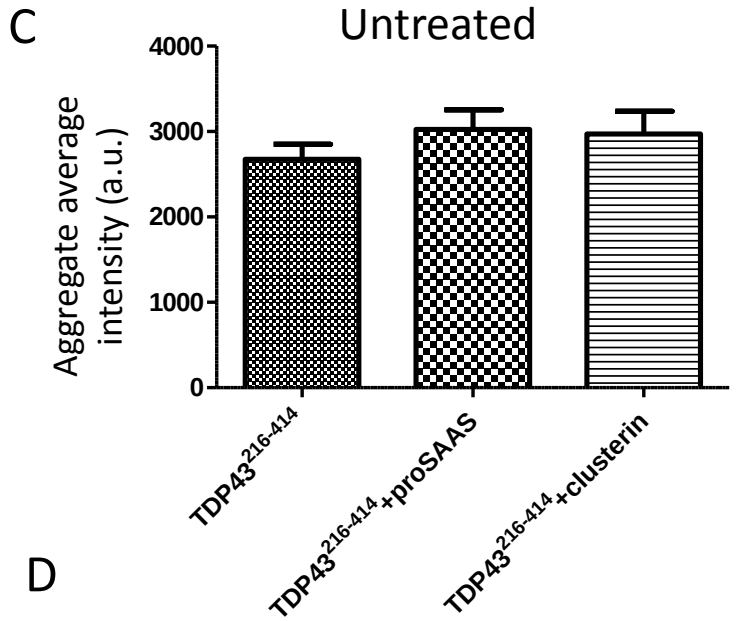
C
Untreated
Aggregate average intensity (a.u.)
4000
3000
2000
1000
0
TDP43216-414
TDP43216-414+proSAAS
TDP43216-414+clusterin

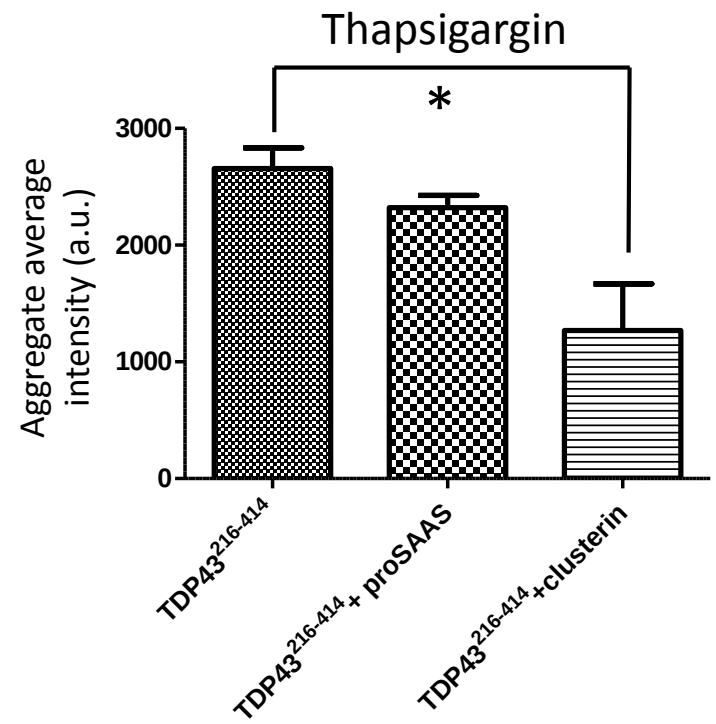
D
Thapsigargin
*
Aggregate average intensity (a.u.)
3000
2000
1000
0
TDP43216-414
TDP43216-414+ proSAAS
TDP43216-414+clusterin

Figure S3

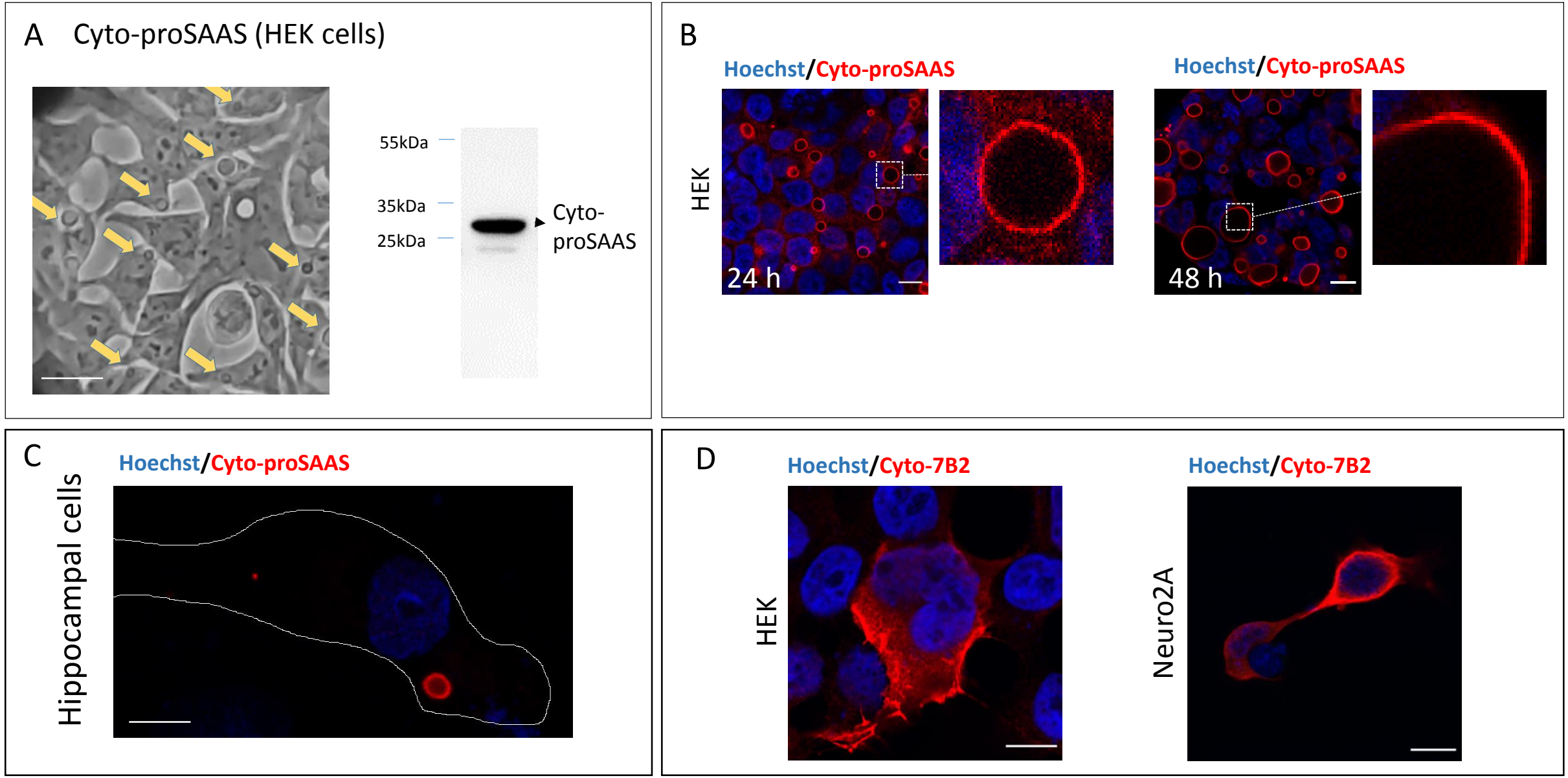
A
Cyto-proSAAS (HEK cells)
55kDa
35kDa
25kDa
Cyto-
proSAAS
B
Hoechst/Cyto-proSAAS
Hoechst/Cyto-proSAAS
HEK
24 h
48 h
C
Hoechst/Cyto-proSAAS
Hippocampal cells
D
Hoechst/Cyto-7B2
Hoechst/Cyto-7B2
HEK
Neuro2A

Figure S4

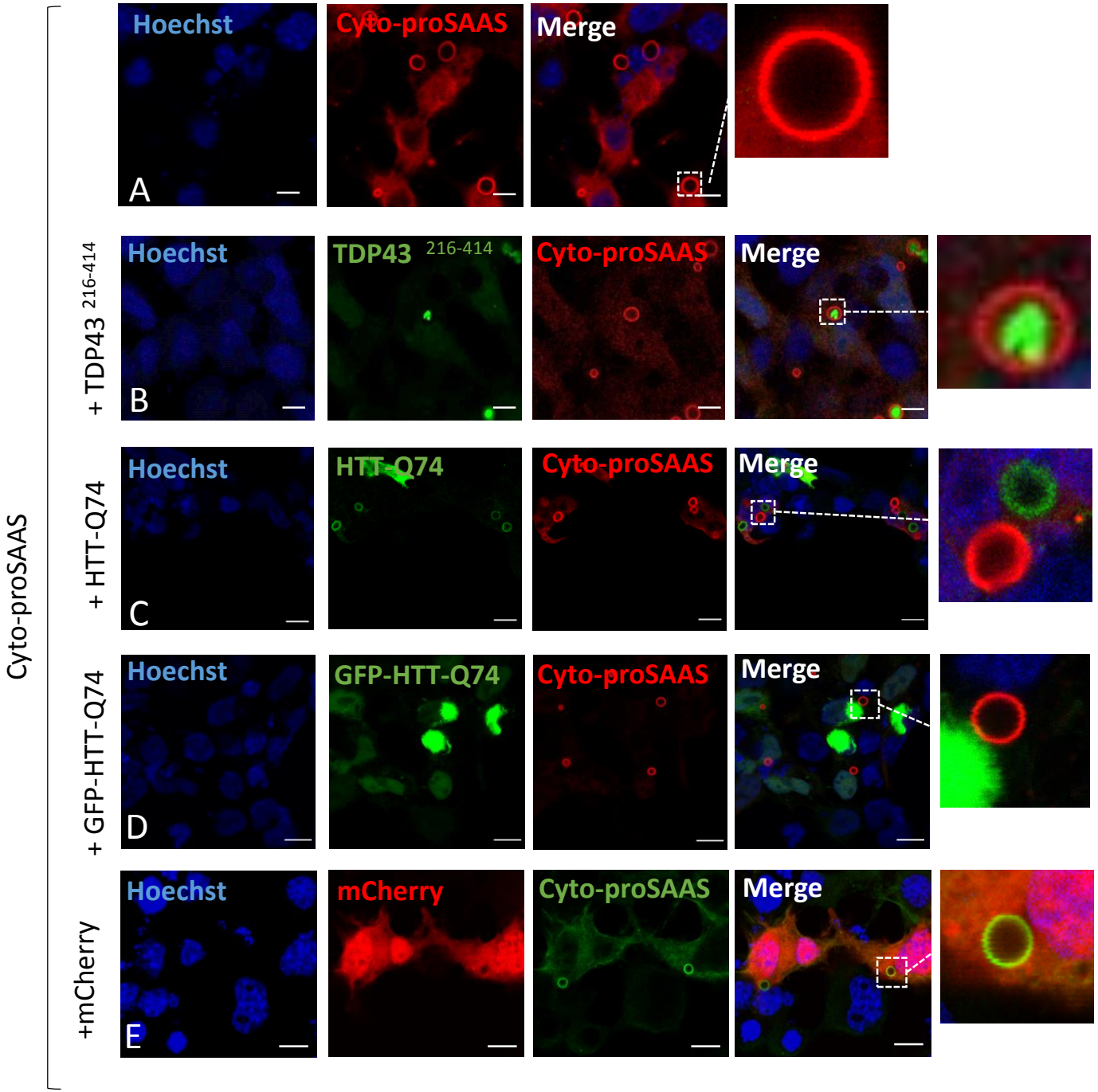
Cyto-proSAAS
Hoechst
Cyto-proSAAS
Merge
A
+ TDP43 216-414
Hoechst
TDP43 216-414
Cyto-proSAAS
Merge
B
+ HTT-Q74
Hoechst
HTT-Q74
Cyto-proSAAS
Merge
C
+ GFP-HTT-Q74
Hoechst
GFP-HTT-Q74
Cyto-proSAAS
Merge
D
+mCherry
Hoechst
mCherry
Cyto-proSAAS
Merge
E

Figure S5

A

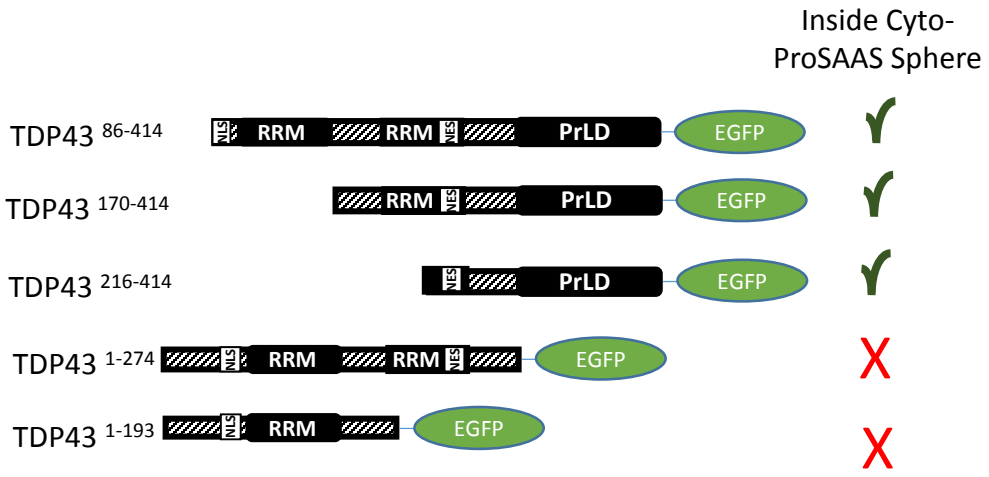

B

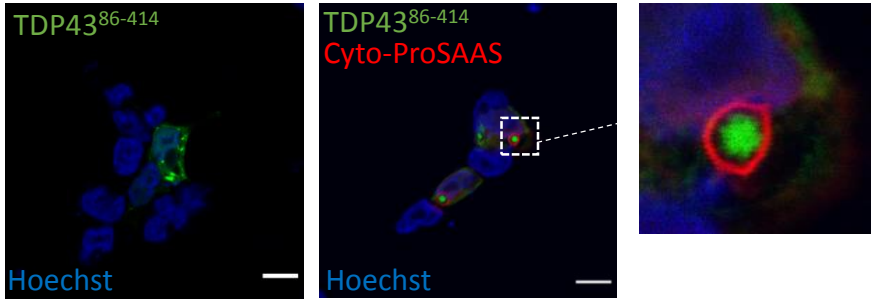

C

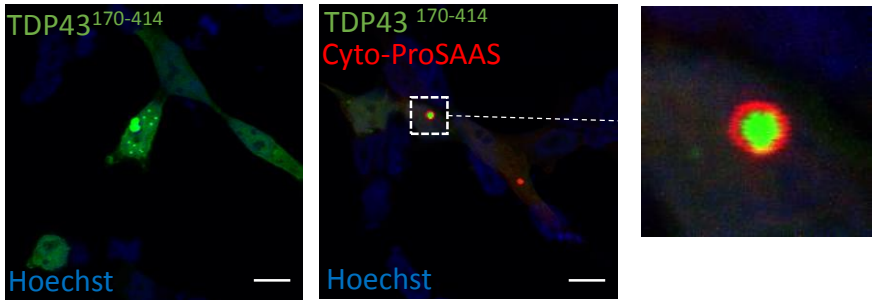

D

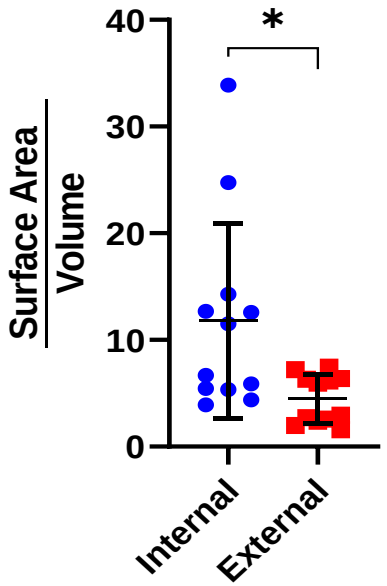

E

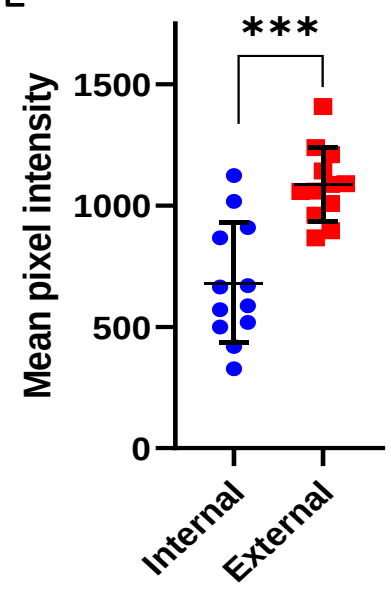

F

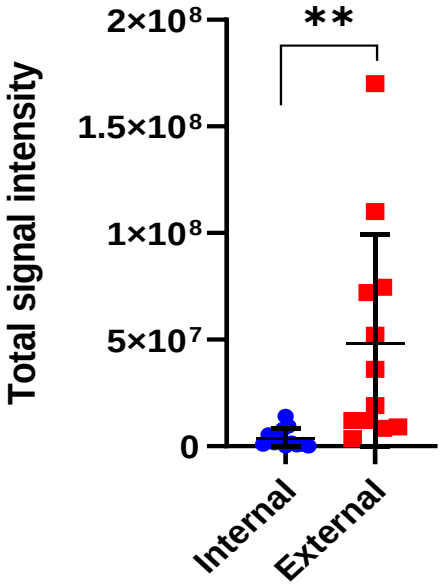

G

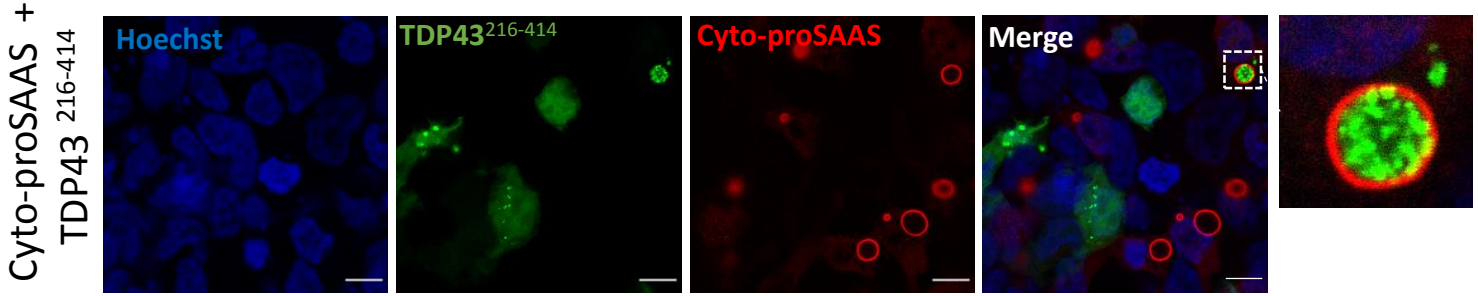

Figure S6

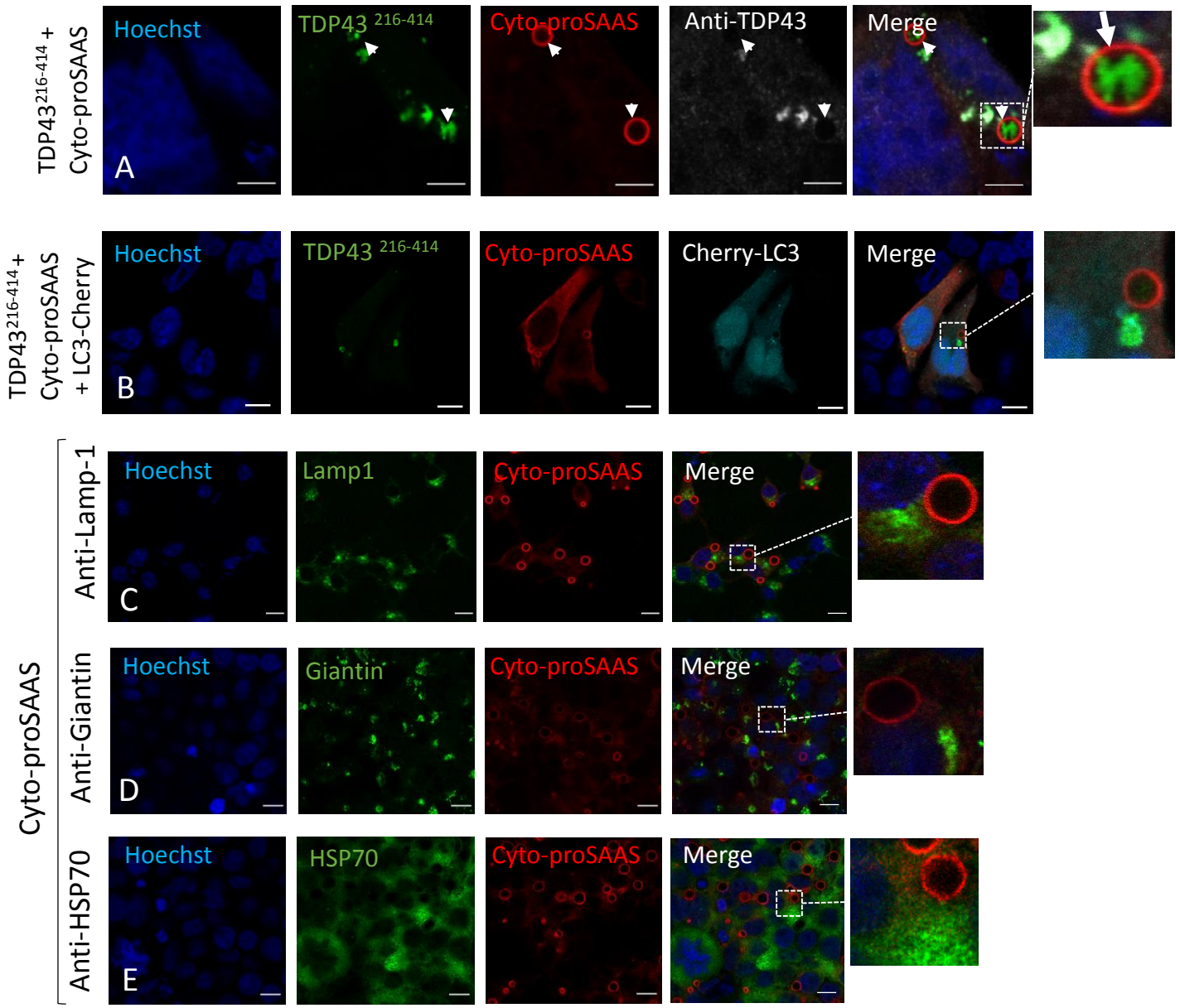
TDP43216-414 + Cyto-proSAAS
Hoechst
TDP43 216-414
Cyto-proSAAS
Anti-TDP43
Merge
A
TDP43216-414 + Cyto-proSAAS + LC3-Cherry
Hoechst
TDP43 216-414
Cyto-proSAAS
Cherry-LC3
Merge
B
Cyto-proSAAS
Anti-Lamp-1
Hoechst
Lamp1
Cyto-proSAAS
Merge
C
Anti-Giantin
Hoechst
Giantin
Cyto-proSAAS
Merge
D
Anti-HSP70
Hoechst
HSP70
Cyto-proSAAS
Merge
E

Figure S7

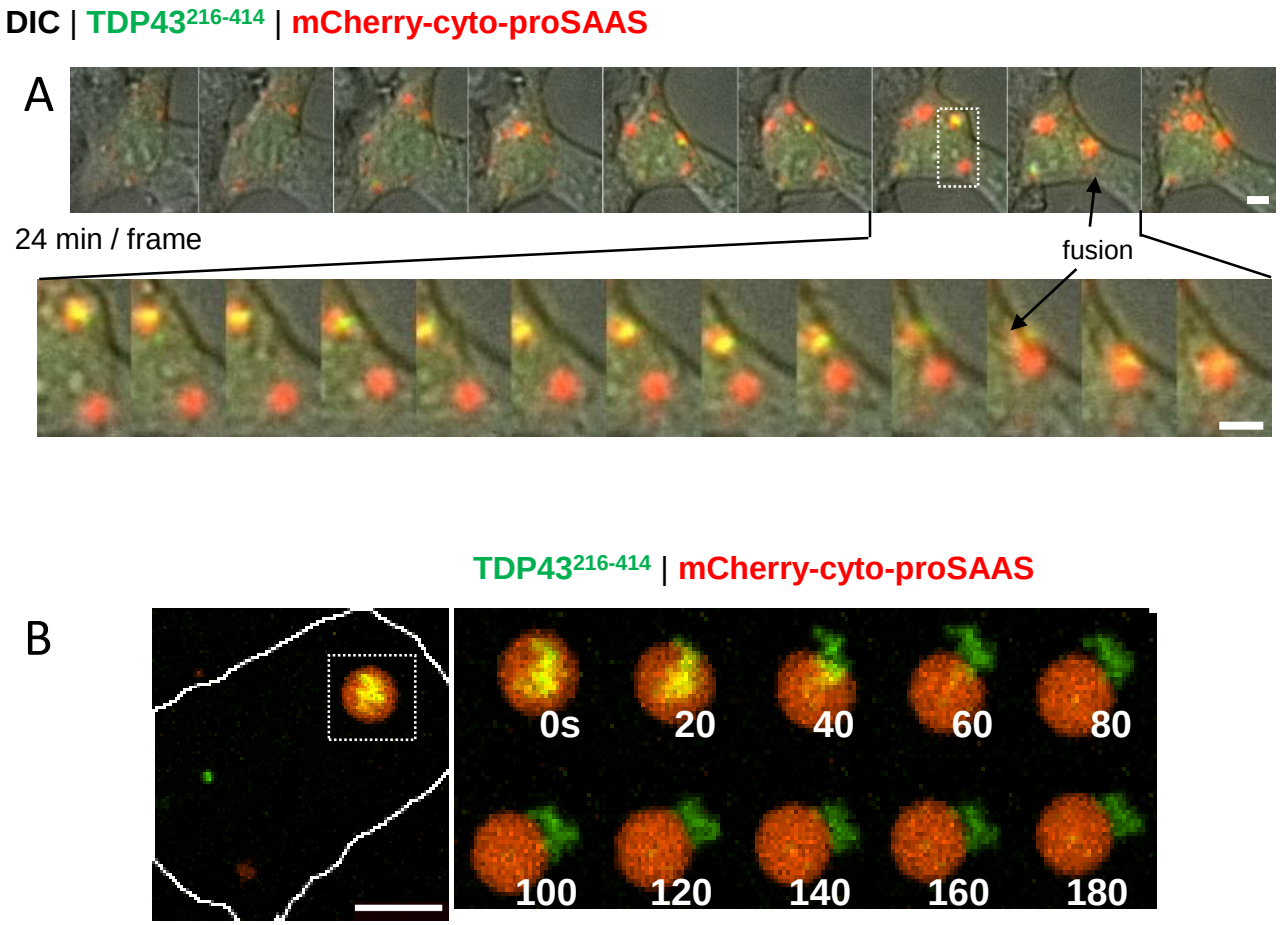
DIC | TDP43216-414 | mCherry-cyto-proSAAS
A
24 min / frame
fusion
TDP43216-414 | mCherry-cyto-proSAAS
B
0s
20
40
60
80
100
120
140
160
180